Development of a mass-preserving level set redistancing algorithm for simulation of rising bubble

Z. H. Gu, H. L. Wen, S. Ye, R. D. An & C. H. Yu

Published online: 22 Jan 2019.

Submit your article to this journal ⧉

Article views: 15

View Crossmark data ⧉

Taylor & Francis
Taylor & Francis Group

Check for updates

Development of a mass-preserving level set redistancing algorithm for simulation of rising bubble

Z. H. Gu[a], H. L. Wen[b], S. Ye[c], R. D. An[d], and C. H. Yu[d]

[a]College of Civil Engineering and Architecture, Zhejiang University, Hangzhou, P. R. China; [b]Department of Engineering Science and Ocean Engineering, National Taiwan University, Taipei, Taiwan, R. O. China; [c]Ocean College, Zhejiang University, Zhoushan, P. R. China; [d]State key lab of Hydraulics and Mountain River Engineering, Sichuan University, Sichuan, P. R. China

ABSTRACT

This article is aimed to simulate the gas-liquid flow of rising bubbles with a mass-preserving level set method. To resolve the topological changes of gas-liquid interface where the classic finite difference scheme may yield oscillation solutions, the spatial terms in the level set advection equation will be approximated by an optimized compact reconstruction weighted essentially non-oscillatory (OCRWENO) scheme. This scheme achieves high-order accuracy in smooth regions, and meanwhile avoid numerical oscillation near discontinuities. Two benchmark problems including vortex flow and deforming field are chosen to compare the present simulation with previous numerical researches. Several rising bubble problems are validated by the proposed level set method.

1. Introduction

Many existing free surface flows in areas of bubble dynamics, water conservancy, coastal and off-shore engineering involve the phenomenon of breaking surface wave. In such complex flows, there exists considerable numerical challenges in simulating motions with large density differences of components at the interface [1]. Level set (LS) methods compared to the Lagrangian-based methods are usually more robust and suitable for modeling the time-evolving free surface with a dramatically varying topology [2,3]. In addition, strong topological changes such as break up and merging of bubbles of incompressible two-phase flows are efficiently simulated even when surface tension needs to be considered [3].

In level set methods [4–7], the interface which separates gas and liquid is defined implicitly as the zero level-set of a continuous signed distance function, which is positive in gas and negative otherwise [8]. Continuity of the continuous level set function has brought about many advantages to level set methods. For example, no reconstruction of the interface is needed, and the interface curvature can be straightforwardly calculated [8]. Son and Dhir simulated film boiling on an immersed solid surface with LS method to solve modified level set formulation. The accurate evaluation of the liquid-vapor interface has been predicted in their scheme [9]. Hwang and Son further applied LS method to particle motion in droplet evaporation through direct numerical simulation (DNS) detailed in [10]. In [11], LS method serves as an important numerical approach to simulating two-dimensional binary droplet collision. A relatively high Weber number is used

<div style="border: 1px solid black">

Nomenclature

u	velocity field	$\bar{S}(\phi_0)$	smoothed sign function
$\delta(\phi)$	Dirac delta function	Δx	grid cell size
$\bar{H}(\phi)$	smoothed Heaviside function	$\mathbf{f}_{sf}$	surface tension force
g	gravitational acceleration	p	pressure
$\kappa(\phi)$	curvature of the interface	$\mu(\phi)$	viscosity
$\rho(\phi)$	density	α	exact wavenumber
α'	numerical wavenumber	β	smoothness indicators
$E(\alpha)$	error function	ω_k	optimized weights
α_k	weights		
ϕ	level set function		

</div>

to understand the mechanism of droplets in which formation of satellite droplets are also investigated. Level set method without resolving the reinitialization process based on the new stabilized finite element approach was proposed in [12] and the corresponding Zalesak's disk and dambreak flow problems were solved. The idea of LS method has been extended to the conservative level set method in premixed turbulent flame simulations [13].

The drawback of the level set approach is due, however, to the introduction of significant numerical dissipation errors in preserving mass conservation. In other words, the discretization of the level set equation results in unnecessary numerical dissipation and then manifests itself as a loss of mass in convex and concave solution regions [14]. The fifth-order weighted essentially non-oscillatory (WENO) scheme for the discretization of level set method is applied to multiphase incompressible flows [15]. The WENO scheme in [16] was extended mainly for the purpose of simulating compressible multiphase flows. On the basis of WENO scheme Kuriokaa and Dowling [17] proposed high-order (7th to 11th) WENO scheme to preserve mass conservation for gas-liquid free surface flows. WENO and its related weighted compact schemes have been the subject of intensive studies for understanding its truncation error, dissipation and dispersion error [18]. Use of WENO scheme for advection equation of level set method was recommended in [19]. The WENO scheme for solving certain types of turbulence or two-phase problems shows that the mass loss is still high due to the dissipation errors [15,20]. Volume-reinitialization scheme which uses volume correction by solving an appropriate equation for level set function after every time step to level set method has been proposed by Salih and Moulic [15].

In comparison with LS method for capturing interface, the coupled level set and volume of fluid (CLSVOF) method proves to be very efficient in numerically modeling interface deformation of bubbles or droplets [21]. In CLSVOF method, the interface is approximated using piecewise linear reconstruction and the normal and curvature of the interface is evaluated from the continuous LS function. Fluid volume fluxes can be therefore calculated from reconstructed interface. The need for reconstructed interface is particularly necessary to reinitialize the LS function for mass conservation. Further improvement in CLSVOF method was studied and applied in [2,3,22–25]. Another hybrid technique for improving mass conservation and calculating curvature is coupled VOF and level set (VOSET) method [26–29]. An iterative geometric approach has been proposed to calculate the level set function with an aim at getting accurate geometric properties. In addition, this methods developed on the basis of VOF approach is adopted to conserve mass.

In contrast to the LS methods developed normally under the re-initialization procedure, conservation level set method makes use of a smoothed Heaviside function instead of signed distance function to predict interface in the compression-diffusion equation [30–32]. In [33–36], the interface which is predicted in Eulerian transport is corrected by introducing Lagrangian markers. This method, called hybrid particle level set (HPLS) method, can refine the original LS method to obtain better mass conservation. The LS method characterized by relating various improvement

techniques has been successfully applied to track the gas/liquid interface including adaptive level set approach [37], structured adaptive mesh refinement [38], refined level set grid (RLSG) method [39], and geometric mass-preserving redistancing scheme [40]. Note that the above three LS methods were developed mainly for the purpose of preserving mass conservation and reducing computational costs.

This article is organized as follows. Section 2 describes governing equations for the incompressible two-phase flow. In Section 3, optimized compact reconstruction weighted essentially non-oscillatory scheme is developed, which accommodates better dispersion relation and avoids numerical oscillation to solve level set evolution equation. Section 4 presents validation of the employed analysis code in vortex flow and deforming field problems. In Section 5, single bubble rising, two-bubble merger and bubble bursting at a free surface with surface tension taken into consideration are investigated to illustrate the scheme's mass conservation property. Concluding remarks are given in Section 6 based on the simulated results.

2. Mathematical model

2.1. Mass-preserving level set redistancing algorithm

2.1.1. Initialization step

The level set function of ϕ_0 which changes from negative (for the gas) to positive (for the liquid) across the interface (zero level set) is reinitialized to a signed distance function ϕ by solving the following re-initialization equation

$$\phi_\tau + \bar{S}(\phi_0)(|\nabla\phi|-1) = 0, \tag{1}$$

where τ is the pseudo-time and $\bar{S}(\phi_0)$ denotes the smoothed sign function

$$\bar{S}(\phi_0) = 2\big(\bar{H}(\phi_0) - 0.5\big), \tag{2}$$

with the smoothed Heaviside function over a finite thickness ε

$$\bar{H}(\phi) = \begin{cases} 0; & \text{if } \phi < -\varepsilon \\ \frac{1}{2}\left[1 + \dfrac{\phi}{\varepsilon} + \dfrac{1}{\pi}\sin\left(\dfrac{\pi\phi}{\varepsilon}\right)\right]; & \text{if } |\phi| \le \varepsilon \\ 1; & \text{if } \phi > \varepsilon. \end{cases} \tag{3}$$

In Eq. (3), ε usually relates to the grid cell size Δx and is chosen to be $\varepsilon = 1.5\Delta x$. A steady-state solution for Eq. (1) can be obtained at time $T = L_D$, which is the largest length of the computational domain when solving Eq. (1). It is noted that an initialization step is performed only once at the initial time, while the following advection and re-initialization steps introduced in Sections 2.1.2 and 2.1.3 respectively are performed at each time step [5].

2.1.2. Advection step

Subject to an initial condition computed form Eq. (1), the following level set evolution equation is considered for the advection of ϕ in a fluid with the velocity field $\mathbf{u}$ [41,42]:

$$\phi_t + \mathbf{u} \cdot \nabla\phi = 0. \tag{4}$$

To solve first derivative terms, one can use a high-resolution scheme such as essentially non-oscillatory (ENO) [43] and weighted essentially non-oscillatory (WENO) [44]. The developed ENO and WENO will inevitably introduce considerable dispersion and dissipation errors and then possibly smear the predicted level set solutions. In other words, the level set function which is defined implicitly $\phi_0(\mathbf{x})$, does not satisfy the condition of signed distance function. This leads

to the problem that curvature of the interface cannot be calculated accurately, and the density and viscosity near the interface cannot be calculated either.

2.1.3. Re-initialization step

To maintain level set function as a signed distance function, we solve the following time-dependent partial differential equation (PDE) from the computed solution ϕ_0 from Eq. (4)

$$\phi_\tau = \bar{S}(\phi_0)(1-|\nabla\phi|) + \lambda f(\phi), \tag{5}$$

with

$$\lambda = -\frac{\int_\Omega \delta(\phi)\big(\bar{S}(\phi_0)(1-|\nabla\phi|)\big)d\Omega}{\int_\Omega \delta(\phi)f(\phi)d\Omega}. \tag{6}$$

Note that the time-dependent λ is derived by requiring mass conservation of the domain as follows

$$\frac{\partial}{\partial t}\int \bar{H}(\phi)\ d\Omega = \int \bar{H}'(\phi)\ \phi_\tau\ d\Omega = \int \bar{H}'(\phi)\ \big[\bar{S}(\phi_0)(1-|\nabla\phi|) + \lambda f(\phi)\big]\ d\Omega = 0. \tag{7}$$

In Eq. (7), the term $f(\phi) = \delta(\phi)|\nabla\phi|$ clearly enlightens that only the interface has been corrected and distance function property can definitely remain undisturbed away from the interface [5]. The Dirac delta function $\delta(\phi)$ in Eq. (6) can be obtained according to the $\frac{d\bar{H}(\phi)}{d\phi}$

$$\delta(\phi) = \begin{cases} \dfrac{1}{2\varepsilon}\left(1 + \cos\left(\dfrac{\pi\phi}{\varepsilon}\right)\right); & \text{if } |\phi| \leq \varepsilon; \\ 0; & \text{otherwise.} \end{cases} \tag{8}$$

While solving this re-initialization equation, it is essential to obtain only the signed distance function within the transition zone using the proposed narrow band level set methods. In other words, only $\frac{\varepsilon}{\Delta t}$ iteration steps are chosen.

2.2. Navier–Stokes equations and physical properties

The fluid velocities $\mathbf{u}$ and pressure p for the two incompressible immiscible fluids are written as

$$\nabla \cdot \mathbf{u} = 0, \tag{9}$$

$$\frac{\partial \mathbf{u}}{\partial t} + \mathbf{u} \cdot \nabla \mathbf{u} = -\frac{1}{\rho}\nabla p + \frac{1}{\rho}\nabla \cdot \left[\mu\left(\nabla\mathbf{u} + (\nabla\mathbf{u})^T\right)\right] + \mathbf{g} + \mathbf{f}_{sf}, \tag{10}$$

where $\mathbf{g}$ is the gravitational acceleration. The other source term in Eq. (10) is the surface tension force $\mathbf{f}_{sf}$, which is modeled using the continuum surface tension (CSF) method [22,45,46]

$$\mathbf{f}_{sf} = \sigma\kappa(\phi)\delta(\phi)\nabla\phi. \tag{11}$$

In Eq. (11), σ is the fluid surface tension coefficient and the curvature of the interface $\kappa(\phi)$ can be defined as

$$\begin{aligned}
\kappa(\phi) &= -\nabla \cdot \left(\frac{\nabla\phi}{|\nabla\phi|}\right) \\
&= -\Big(\phi_x^2\phi_{yy} - 2\phi_x\phi_y\phi_{xy} + \phi_y^2\phi_{xx} + \phi_x^2\phi_{zz} - 2\phi_x\phi_z\phi_{xz} + \phi_z^2\phi_{xx} \\
&\quad + \phi_y^2\phi_{zz} - 2\phi_y\phi_z\phi_{yz} + \phi_z^2\phi_{yy}\Big)\Big/\left(\phi_x^2 + \phi_y^2 + \phi_z^2\right)^{\frac{3}{2}}.
\end{aligned} \tag{12}$$

The first and second derivative terms of level set function in the above mean curvature Eq. (12) are discretized using the second-order accurate central difference scheme. In Eq. (10), the physical properties density ρ and viscosity μ will be smoothly approximated through smoothed Heaviside function to resolve the contact discontinuity oscillations at the interface

$$\begin{aligned} \rho(\phi) &= \rho_G + (\rho_L - \rho_G)\bar{H}(\phi), \\ \mu(\phi) &= \mu_G + (\mu_L - \mu_G)\bar{H}(\phi), \end{aligned} \tag{13}$$

where the subscripts G and L correspond to gas and liquid, respectively.

3. Numerical scheme

Uniform grid spacings with $\Delta x = \Delta y = \Delta z = h$ are adopted in the proposed two-phase flow solver. With a staggered grid arrangement, the discrete level set function ϕ and pressure p are located at cell centers while the discrete velocity field $\mathbf{u}$ is located at cell faces.

3.1. Level set method solver

3.1.1. Time marching scheme for the level set evolution equation

The level set evolution equation introduced in Section 2.1.2, can be written in conservative form since $\mathbf{u}$ is a solenoidal vector field, namely,

$$\phi_t + \nabla \cdot (\mathbf{u}\phi) = 0. \tag{14}$$

Using a semi-discrete conservative finite difference scheme for Eq. (14) results in an ordinary differential equation (ODE)

$$\frac{d\phi_{i,j}}{dt} = L(\phi_{i,j}) = -\frac{1}{\Delta x}\left(F_{i+\frac{1}{2}j} - F_{i-\frac{1}{2}j}\right) - \frac{1}{\Delta y}\left(G_{i,j+\frac{1}{2}} - G_{i,j-\frac{1}{2}}\right) \tag{15}$$

where $F = \phi u$ and $G = \phi v$. The convective flux term shown in Eq. (15) is approximated in conservative form by OCRWENO scheme introduced in Section 3.1.2 to achieve fourth-order accuracy in smooth regions and avoid oscillations near discontinuities. Given the initial solution $\phi^{(n)}$, the solution at next time step $\phi^{(n+1)}$ can be obtained using a total variation diminishing third-order Runge–Kutta (TVD-RK3) scheme for Eq. (14)

$$\phi^{(1)} = \phi^{(n)} + \Delta t L\left(\phi^{(0)}\right), \tag{16}$$

$$\phi^{(2)} = \frac{3}{4}\phi^{(n)} + \frac{1}{4}\phi^{(1)} + \frac{1}{4}\Delta t L\left(\phi^{(1)}\right), \tag{17}$$

$$\phi^{(n+1)} = \frac{1}{3}\phi^{(n)} + \frac{2}{3}\phi^{(2)} + \frac{2}{3}\Delta t L\left(\phi^{(2)}\right). \tag{18}$$

3.1.2. Approximation of spatial derivatives for the level set evolution equation

3.1.2.1. Optimized upwind compact difference scheme.

Upwinding compact difference (UCD) scheme with higher accuracy is a critical numerical tool to simulate fluid flow problems. Owing to its capability in saving considerable computational costs with higher accuracy solutions in fewer grid points, compact schemes have been intensively studied for various applications such as direct numerical simulation, acoustics and hypersonic boundary-layer transition [47–50]. In this section, progress towards refining the UCD scheme has made this scheme a better dispersion-relation-preserving (DRP) property [51–55] to simulate the two-phase fluid flows over a considerable wavenumber range.

The first-order derivative term $\frac{\partial \phi}{\partial x}$ will be approximated using the positive convective coefficient by the following implicit UCD scheme:

$$\bar{A} \frac{\partial \phi}{\partial x}\bigg|_{i-1} + \frac{\partial \phi}{\partial x}\bigg|_{i} + \bar{C} \frac{\partial \phi}{\partial x}\bigg|_{i+1} = \frac{\bar{a}\phi_{i-2} + \bar{b}\phi_{i-1} + \bar{c}\phi_i + \bar{d}\phi_{i+1}}{\Delta x}. \tag{19}$$

The modified equation analysis is applied in Eq. (19) to derive the following set of algebraic equations

$$\bar{a} + \bar{b} + \bar{c} + \bar{d} = 0, \tag{20}$$

$$-2\bar{a} - \bar{b} + \bar{d} - \bar{A} - \bar{C} = 1, \tag{21}$$

$$2\bar{a} + \frac{1}{2}\bar{b} + \frac{1}{2}\bar{d} + \bar{A} - \bar{C} = 0, \tag{22}$$

$$-\frac{4}{3}\bar{a} - \frac{1}{6}\bar{b} + \frac{1}{6}\bar{d} - \frac{1}{2}\bar{A} - \frac{1}{2}\bar{C} = 0, \tag{23}$$

$$\frac{2}{3}\bar{a} + \frac{1}{24}\bar{b} + \frac{1}{24}\bar{d} + \frac{1}{6}\bar{A} - \frac{1}{6}\bar{C} = 0, \tag{24}$$

$$-\frac{4}{15}\bar{a} - \frac{1}{120}\bar{b} + \frac{1}{120}\bar{d} - \frac{1}{24}\bar{A} - \frac{1}{24}\bar{C} = 0. \tag{25}$$

The unknown coefficients shown in Eq. (19) are then determined as follows: $\bar{A} = \frac{1}{2}$, $\bar{C} = \frac{1}{6}$, $\bar{a} = -\frac{1}{18}$, $\bar{b} = -1$, $\bar{c} = \frac{1}{2}$, and $\bar{d} = \frac{5}{9}$. These derived coefficients can be applied to get the fifth-order spatial accuracy of the first-order derivative term

$$\frac{\partial \phi}{\partial x} = \frac{\partial \phi}{\partial x}\bigg|_{exact} + \frac{1}{60}\Delta x^5 \frac{\partial^6 \phi}{\partial x^6} + O(\Delta x^6). \tag{26}$$

It is remarkable to point out here that the use of DRP finite difference approximation for the first derivative term $\frac{\partial \phi}{\partial x}$ in wavenumber space can preserve the dispersive nature or reduce the dispersion errors as much as possible [51]. We perform a modified number approach on each term shown in Eq. (19)

$$\mathbf{i}\alpha'\Delta x(\bar{A}\mathbf{e}^{-\mathbf{i}\alpha\Delta x} + 1 + \bar{C}\mathbf{e}^{\mathbf{i}\alpha\Delta x}) = \bar{a}\mathbf{e}^{-2\mathbf{i}\alpha\Delta x} + \bar{b}\mathbf{e}^{-\mathbf{i}\alpha\Delta x} + \bar{c} + \bar{d}\mathbf{e}^{\mathbf{i}\alpha.\Delta x}. \tag{27}$$

As a result, the numerical wavenumber $\alpha'\Delta x$ can be determined by solving the Eq. (27)

$$\alpha'\Delta x = \frac{\mathbf{i}(-3\mathbf{e}^{-2\mathbf{i}\alpha\Delta x} + 4\mathbf{e}^{-2\mathbf{i}\alpha\Delta x}\bar{d} - 24\mathbf{e}^{-\mathbf{i}\alpha\Delta x} + 18\mathbf{e}^{-\mathbf{i}\alpha\Delta x}\bar{d} + 27 - 36\bar{d} + 14\bar{d}\mathbf{e}^{\mathbf{i}\alpha\Delta x})}{-14 - 17\mathbf{e}^{-\mathbf{i}\alpha\Delta x} + 18\mathbf{e}^{-\mathbf{i}\alpha\Delta x}\bar{d} + \mathbf{e}^{\mathbf{i}\alpha\Delta x} - 6\bar{d}\mathbf{e}^{\mathbf{i}\alpha\Delta x}}. \tag{28}$$

Then, we define the error function E which minimizes the L_2 norm of the difference between the numerical wavenumber $\alpha'\Delta x$ and the exact wavenumber $\alpha\Delta x$ over the particular wave number range 0 and $\mathbf{e}$

$$E(\alpha) = \int_0^{\mathbf{e}} [W \cdot (\alpha\Delta x - \Re[\alpha'\Delta x])]^2 d(\alpha\Delta x), \tag{29}$$

where W is the denominator of $(\alpha\Delta x - \Re[\alpha'\Delta x])$. In Eq. (29), the value $\mathbf{e}$ is recommended to be chosen as $\mathbf{e} = \frac{17\pi}{20}$ according to the dispersion analysis for comparison [51]. To determine the optimized coefficients in Eq. (19), the constraint equation for $\frac{\partial E}{\partial \bar{d}} = 0$ is solved together with five algebraic equations shown in Eqs. (20)–(24). We obtain the optimized coefficients: $\bar{A} = 0.5418416108$, $\bar{C} = 0.1527194630$, $\bar{a} = -0.0648536914$, $\bar{b} = -1.041841611$, $\bar{c} = 0.583683223$, and $\bar{d} = 0.5230120803$. Use of the above optimized coefficients enables us to get a solution that can theoretically reduce dispersion errors. Define the values at cell faces $i \pm \frac{1}{2}$ as follows:

$$\tilde{A}\hat{\phi}_{i-\frac{1}{2}} + \hat{\phi}_{i+\frac{1}{2}} + \tilde{C}\hat{\phi}_{i+\frac{3}{2}} = \tilde{a}\phi_{i-1} + \tilde{b}\phi_i + \tilde{c}\phi_{i+1}, \tag{30}$$

and

$$\tilde{A}\hat{\phi}_{i-\frac{3}{2}} + \hat{\phi}_{i-\frac{1}{2}} + \tilde{C}\hat{\phi}_{i+\frac{1}{2}} = \tilde{a}\phi_{i-2} + \tilde{b}\phi_{i-1} + \tilde{c}\phi_i. \tag{31}$$

The coefficients $\tilde{A} = 0.541841611, \tilde{C} = 0.152719463, \tilde{a} = 0.064853691, \tilde{b} = 1.106695303$, and $\tilde{c} = 0.523012080$ are then derived by comparing the optimized coefficients derived in Eq. (19) with $\frac{\partial\phi}{\partial x}$.

3.1.2.2. OCRWENO4 scheme. To efficiently eliminate the spurious oscillations in the vicinity of discontinuities of solutions, WENO schemes [56] can be applied. Investigation of WENO schemes produces commonly dispersion and dissipation errors for simulation of turbulent flow [20]. The proposed OCRWENO scheme is useful in preventing nonphysical oscillations across discontinuities and improving dispersion and dissipation properties in smooth regions.

A fifth-order compact reconstruction scheme weighted ENO (CRWENO) scheme for hyperbolic conservation law was proposed by Ghosh and Baeder in 2012 [57]. The CRWENO scheme developed in their study will be further extended in this paper with dispersion-relation-preserving property. Here, first of all we construct three third-order compact interpolations as alternatives

$$\frac{2}{3}\hat{\phi}_{i-\frac{1}{2}} + \frac{1}{3}\hat{\phi}_{i+\frac{1}{2}} = \frac{1}{6}(\phi_{i-1} + 5\phi_i), \tag{32}$$

$$\frac{1}{3}\hat{\phi}_{i-\frac{1}{2}} + \frac{2}{3}\hat{\phi}_{i+\frac{1}{2}} = \frac{1}{6}(5\phi_i + \phi_{i+1}), \tag{33}$$

$$\frac{2}{3}\hat{\phi}_{i+\frac{1}{2}} + \frac{1}{3}\hat{\phi}_{i+\frac{3}{2}} = \frac{1}{6}(\phi_i + 5\phi_{i+1}). \tag{34}$$

The flux values of $\hat{\phi}$ at the half points given below will be adopted to solve level set evolution equation from the above combination of three third-order compact interpolations that are sequentially multiplied by coefficients c_i for $i = 1–3$:

$$\left[\frac{2c_1 + c_2}{3}\right]\hat{\phi}_{i-\frac{1}{2}} + \left[\frac{c_1 + 2(c_2 + c_3)}{3}\right]\hat{\phi}_{i+\frac{1}{2}} + \frac{c_3}{3}\hat{\phi}_{i+\frac{3}{2}}$$
$$= \frac{c_1}{6}\phi_{i-1} + \left[\frac{5(c_1 + c_2) + c_3}{6}\right]\phi_i + \left[\frac{c_2 + 5c_3}{6}\right]\phi_{i+1}. \tag{35}$$

Values of $c_1 = 0.20891, c_2 = 0.5$, and $c_3 = 0.29109$ are then obtained by comparing the coefficients derived in Eq. (30). Thanks to the idea of a WENO scheme [44], we are led to know that the general form of the interface $\hat{\phi}$ reconstructed using a left-biased interpolation is

$$\left[\frac{2\omega_1 + \omega_2}{3}\right]\hat{\phi}_{i-\frac{1}{2}}^L + \left[\frac{\omega_1 + 2(\omega_2 + \omega_3)}{3}\right]\hat{\phi}_{i+\frac{1}{2}}^L + \frac{\omega_3}{3}\hat{\phi}_{i+\frac{3}{2}}^L$$
$$= \frac{\omega_1}{6}\phi_{i-1} + \left[\frac{5(\omega_1 + \omega_2) + \omega_3}{6}\right]\phi_i + \left[\frac{\omega_2 + 5\omega_3}{6}\right]\phi_{i+1}. \tag{36}$$

ω_k in Eq. (36) is the weight of k-th stencil in the convex combination, which are defined as

$$\omega_k = \frac{\alpha_k}{\sum_k \alpha_k}, \quad k = 1, 2, 3, \tag{37}$$

where α_k in the above equation is determined by smoothness indicators $\tilde{\beta}_k$ of the respective stencils

$$\tilde{\alpha}_k = \frac{\tilde{c}_k}{\left(\tilde{\beta}_k + \epsilon\right)^2}, \quad k = 1, 2, 3, \tag{38}$$

and $\epsilon = 10^{-6}$ is adopted to avoid the denominator becoming zero. To detect large discontinuities, the smoothness indicators $\tilde{\beta}_k$ are given by [44]

$$\beta_1 = \frac{13}{12}(\phi_{i-2}-2\phi_{i-1} + \phi_i)^2 + \frac{1}{4}(\phi_{i-2}-4\phi_{i-1} + 3\phi_i)^2,$$
$$\beta_2 = \frac{13}{12}(\phi_{i-1}-2\phi_i + \phi_{i+1})^2 + \frac{1}{4}(\phi_{i-1}-\phi_{i+1})^2, \tag{39}$$
$$\beta_3 = \frac{13}{12}(\phi_i-2\phi_{i+1} + \phi_{i+2})^2 + \frac{1}{4}(3\phi_i-4\phi_{i+1} + \phi_{i+2})^2.$$

Given the need of designing a weight α_k that can reduce excessive dissipation, the following α_k for the Eq. (38) is redefined [58] in this study, leading to

$$\alpha_k = c_k \left(1 + \frac{|\beta_3 - \beta_1|}{\epsilon + \beta_k}\right), \quad k = 1, 2, 3. \tag{40}$$

For cases with right-biased interpolation, the OCRWENO scheme is also followed by introducing the optimized weights $\tilde{\omega}_k$ for the approximation

$$\left[\frac{2\tilde{\omega}_1 + \tilde{\omega}_2}{3}\right]\hat{\phi}_{i+\frac{3}{2}}^R + \left[\frac{\tilde{\omega}_1 + 2(\tilde{\omega}_2 + \tilde{\omega}_3)}{3}\right]\hat{\phi}_{i+\frac{1}{2}}^R + \frac{\tilde{\omega}_3}{3}\hat{\phi}_{i-\frac{1}{2}}^R$$
$$= \frac{\tilde{\omega}_1}{6}\phi_{i+2} + \left[\frac{5(\tilde{\omega}_1 + \tilde{\omega}_2) + \tilde{\omega}_3}{6}\right]\phi_{i+1} + \left[\frac{\tilde{\omega}_2 + 5\tilde{\omega}_3}{6}\right]\phi_i, \tag{41}$$

where

$$\tilde{\omega}_k = \frac{\tilde{\alpha}_k}{\sum_k \tilde{\alpha}_k}, \quad \tilde{\alpha}_k = c_k \left(1 + \frac{|\tilde{\beta}_3 - \tilde{\beta}_1|}{\epsilon + \tilde{\beta}_k}\right), \quad k = 1, 2, 3, \tag{42}$$

and

$$\tilde{\beta}_1 = \frac{13}{12}(\phi_{i+1}-2\phi_{i+2} + \phi_{i+3})^2 + \frac{1}{4}(3\phi_{i+1}-4\phi_{i+2} + \phi_{i+3})^2,$$
$$\tilde{\beta}_2 = \frac{13}{12}(\phi_i-2\phi_{i+1} + \phi_{i+2})^2 + \frac{1}{4}(\phi_i-\phi_{i+2})^2, \tag{43}$$
$$\tilde{\beta}_3 = \frac{13}{12}(\phi_{i-1}-2\phi_i + \phi_{i+1})^2 + \frac{1}{4}(\phi_{i-1}-4\phi_i + 3\phi_{i+1})^2.$$

The approximation of the convection term $\frac{\partial(u\phi)}{\partial x}$ in the level set evolution equation is to conserve the flux term $u\phi$ across a cell of length Δx by means of

$$\frac{\partial(u\phi)}{\partial x} = \frac{u_{i+\frac{1}{2}}\hat{\phi}_{i+\frac{1}{2}}-u_{i-\frac{1}{2}}\hat{\phi}_{i-\frac{1}{2}}}{\Delta x} \tag{44}$$

where

$$\hat{\phi}_{i+1/2} = \begin{cases} \hat{\phi}_{i+1/2}^L & \text{if } u_{i-\frac{1}{2}} \geq 0, \\ \hat{\phi}_{i+1/2}^R & \text{if } u_{i+\frac{1}{2}} < 0. \end{cases} \tag{45}$$

For the proposed OCRWENO scheme based on the right-biased interpolation, the numerical flux terms at the left and right half boundary point $\frac{1}{2}$ and $N + \frac{1}{2}$ are approximated by the following formula, respectively

$$\hat{\phi}_{i+\frac{1}{2}}^L = \frac{\omega_1}{3}\phi_{i-2}-\frac{1}{6}(7\omega_1 + \omega_2)\phi_{i-1} + \frac{1}{6}(11\omega_1 + 5\omega_2 + 2\omega_3)\phi_i$$
$$+ \frac{1}{6}(2\omega_2 + 5\omega_3)\phi_{i+1}-\frac{\omega_3}{6}\phi_{i+2},$$
$$\hat{\phi}_{i+\frac{1}{2}}^R = -\frac{\tilde{\omega}_3}{6}\phi_{i-1} + \frac{1}{6}(2\tilde{\omega}_2 + 5\tilde{\omega}_3)\phi_i + \frac{1}{6}(11\tilde{\omega}_1 + 5\tilde{\omega}_2 + 2\tilde{\omega}_3)\phi_{i+1}$$
$$-\frac{1}{6}(7\tilde{\omega}_1 + \tilde{\omega}_2)\phi_{i+2} + \frac{\tilde{\omega}_1}{3}\phi_{i+3}, \tag{46}$$

where ω and $\tilde{\omega}$ are defined in Eqs. (37) and (38), respectively. In this study the chosen numerical fluxes at the boundary interfaces expressed in Eq. (46) are reconstructed using the fifth-order

accurate WENO scheme of Jiang and Shu [44]. The proposed OCRWENO scheme, which uses Eq. (46) for $i = 0$ and $N + 1$, Eq. (36) for $i = 1, 3, 4.., N$ forms a tridiagonal matrix system and can be represented as

$$
\begin{bmatrix}
1 & 0 & 0 & ... & ... & ... & 0 \\
a & b & c & 0 & ... & ... & 0 \\
. & & . & & & & . \\
. & & & . & & & . \\
. & & & & . & & . \\
0 & ... & ... & 0 & a & b & c \\
0 & ... & ... & ... & 0 & 0 & 1
\end{bmatrix}
\begin{bmatrix}
\hat{\phi}_{1/2} \\
. \\
. \\
\hat{\phi}_{i+1/2} \\
. \\
. \\
\hat{\phi}_{N+1/2}
\end{bmatrix}
=
\begin{bmatrix}
\bar{r}_{1/2}^{WENO5} \\
. \\
. \\
\bar{r}_{i+1/2}^{OCRWENO4} \\
. \\
. \\
\bar{r}_{N+1/2}^{WENO5}
\end{bmatrix},
\tag{47}
$$

where a, b, c are the coefficients, as shown in Eqs. (36) and (41). It is noted that $\bar{r}_{i+1/2}^{OCRWENO4}$ and $\bar{r}_{1/2}^{WENO5}$ are the right-hand side of the reconstruction flux shown in Eq. (36), (41), or (46), respectively.

3.1.3. Approximation of re-initialization equation

In two-dimensional cases, Eq. (5) can be expressed in a semi-discrete form:

$$
\frac{d\phi}{dt} + H_G\left(\phi_x^+, \phi_x^-, \phi_y^+, \phi_y^-\right) = 0,
\tag{48}
$$

where H_G is the Godunov Hamiltonian. The time marching scheme for the re-initialization Eq. (48) is based on the TVD-RK3 scheme that is described in Section 3.1.1. The time step $\Delta\tau$ in this paper is chosen as $0.25\Delta x$.

Denote $\triangle^+\phi_k = \phi_{k+1} - \phi_k, \triangle^-\phi_k = \phi_k - \phi_{k-1}(k = i-3 \sim i+2)$, and we can obtain the fifth-order WENO5 scheme as [59]

$$
\phi_{x,i}^- = \frac{1}{12}\left(-\frac{\triangle^+\phi_{i-2}}{\triangle x} + 7\frac{\triangle^+\phi_{i-1}}{\triangle x} + 7\frac{\triangle^+\phi_i}{\triangle x} - \frac{\triangle^+\phi_{i+1}}{\triangle x}\right) \\
- \phi^{WENO}\left(\frac{\triangle^-\triangle^+\phi_{i-2}}{\triangle x}, \frac{\triangle^-\triangle^+\phi_{i-1}}{\triangle x}, \frac{\triangle^-\triangle^+\phi_i}{\triangle x}, \frac{\triangle^-\triangle^+\phi_{i+1}}{\triangle x}\right),
\tag{49}
$$

and

$$
\phi_{x,i}^+ = \frac{1}{12}\left(-\frac{\triangle^+\phi_{i-2}}{\triangle x} + 7\frac{\triangle^+\phi_{i-1}}{\triangle x} + 7\frac{\triangle^+\phi_i}{\triangle x} - \frac{\triangle^+\phi_{i+1}}{\triangle x}\right) \\
- \phi^{WENO}\left(\frac{\triangle^-\triangle^+\phi_{i+2}}{\triangle x}, \frac{\triangle^-\triangle^+\phi_{i+1}}{\triangle x}, \frac{\triangle^-\triangle^+\phi_i}{\triangle x}, \frac{\triangle^-\triangle^+\phi_{i-1}}{\triangle x}\right).
\tag{50}
$$

It can be evidently seen that the above spatial discretization of $\phi_{x,i}^-$ and $\phi_{x,i}^+$ is left-biased stencil from $i-3$ to $i+2$ and right-biased stencil from $i-2$ to $i+3$, respectively. The second term ϕ^{WENO} on the right hand side is nonlinear and can be expressed as follows in terms of $\mathbf{a}, \mathbf{b}, \mathbf{c}, \mathbf{d}$:

$$
\phi^{WENO}(\mathbf{a}, \mathbf{b}, \mathbf{c}, \mathbf{d}) = \frac{1}{3}\bar{\omega}_0(\mathbf{a} - 2\mathbf{b} + \mathbf{c}) + \frac{1}{6}\left(\bar{\omega}_2 - \frac{1}{2}\right)(\mathbf{b} - 2\mathbf{c} + \mathbf{d}).
\tag{51}
$$

The weighting factors $\bar{\omega}_0$ and $\bar{\omega}_2$ can be obtained as

$$
\bar{\omega}_0 = \frac{\alpha_0}{\alpha_0 + \alpha_1 + \alpha_2}, \bar{\omega}_2 = \frac{\alpha_2}{\alpha_0 + \alpha_1 + \alpha_2},
\tag{52}
$$

with

$$
\alpha_0 = \frac{1}{(\varepsilon + IS_0)^2}, \alpha_1 = \frac{6}{(\varepsilon + IS_1)^2}, \alpha_2 = \frac{3}{(\varepsilon + IS_2)^2},
\tag{53}
$$

where ε is chosen to prevent the occurrence of division by zero based on the suggestion of Jiang and Shu [44]. The smoothness indicators are defined as follows:

$$
\begin{aligned}
IS_0 &= 13(\mathbf{a}-\mathbf{b})^2 + 3(\mathbf{a}-3\mathbf{b})^2, \\
IS_1 &= 13(\mathbf{b}-\mathbf{c})^2 + 3(\mathbf{b}+\mathbf{c})^2, \\
IS_2 &= 13(\mathbf{c}-\mathbf{d})^2 + 3(3\mathbf{c}-\mathbf{d})^2.
\end{aligned}
\tag{54}
$$

Define $(\bar{a})^+ = \max(a,0), (\bar{a})^- = -\min(a,0)$ and the same subscripts for b, c and d, and $|\nabla\phi|$ in Eq. (6) can be computed using Godunov's method [59]

$$
|\nabla\phi| = \begin{cases}
\bar{S}(\phi_0)\left(\sqrt{\left[\max\left(\bar{a}^-,\bar{b}^+\right)\right]^2 + \left[\max\left(\bar{c}^-,\bar{d}^+\right)\right]^2}\right); & \text{if } \phi_0 \geq 0, \\
\bar{S}(\phi_0)\left(\sqrt{\left[\max\left(\bar{a}^+,\bar{b}^-\right)\right]^2 + \left[\max\left(\bar{c}^+,\bar{d}^-\right)\right]^2}\right); & \text{otherwise.}
\end{cases}
\tag{55}
$$

Sussman and Fatemi [5] used a nine-point stencil to perform numerical integration over the domain $\Omega_{i,j}$ in the Eq. (6)

$$
\int_{\Omega_{ij}} g \approx \frac{h^2}{24}\left(16g_{ij} + \sum_{m,n=-1;(m,n)\neq(0,0)}^{1} g_{i+m,j+n}\right).
\tag{56}
$$

In three-dimensional cases, the 27-point stencil was used as well to compute numerical integration over the domain $\Omega_{i,j,k}$

$$
\int_{\Omega_{ijk}} g \approx 51g_{ijk} + \sum_{m,n,l=-1;(m,n,l)\neq(0,0,0)}^{1} g_{i+m,j+n,k+l}.
\tag{57}
$$

3.2. Navier–Stokes equation solver

3.2.1. Approximation of the advection and diffusion terms

When solving the convection-diffusion flow equations, the upwind principle is considered to reduce numerical oscillations. Take the convection terms $u\frac{\partial u}{\partial x}$ in the x-direction momentum equation as an example. The resulting discretized formula is written as follows for a second-order upwinding scheme:

$$
u\frac{\partial u}{\partial x} = \frac{1}{2}\left(u^+\left(3u_{i,j,k}-4u_{i-1,j,k}+u_{i-2,j,k}\right) + u^-\left(-u_{i+2,j,k}+4u_{i+1,j,k}-3u_{i,j,k}\right)\right),
\tag{58}
$$

where $u^+ = \frac{1}{2}\left(u_{i,j,k}+|u_{i,j,k}|\right)$ and $u^- = \frac{1}{2}\left(u_{i,j,k}-|u_{i,j,k}|\right)$. The four-point third-order upwinding finite difference scheme is also taken into account to approximate advection terms in the simulation of Navier–Stokes equation. That is,

$$
u\frac{\partial u}{\partial x} = \frac{1}{6\Delta x}\left(u^+\left(11u_{i,j,k}-18u_{i-1,j,k}+9u_{i-2,j,k}-2u_{i-3,j,k}\right) + u^-\left(2u_{i+3,j,k}-9u_{i+2,j,k}+18u_{i+1,j,k}-11u_{i,j,k}\right)\right).
\tag{59}
$$

In our computation test, the second-order upwinding scheme is applied in this study when there is enough grid resolution for the advection terms. The diffusion terms are approximated by the second-order center difference scheme.
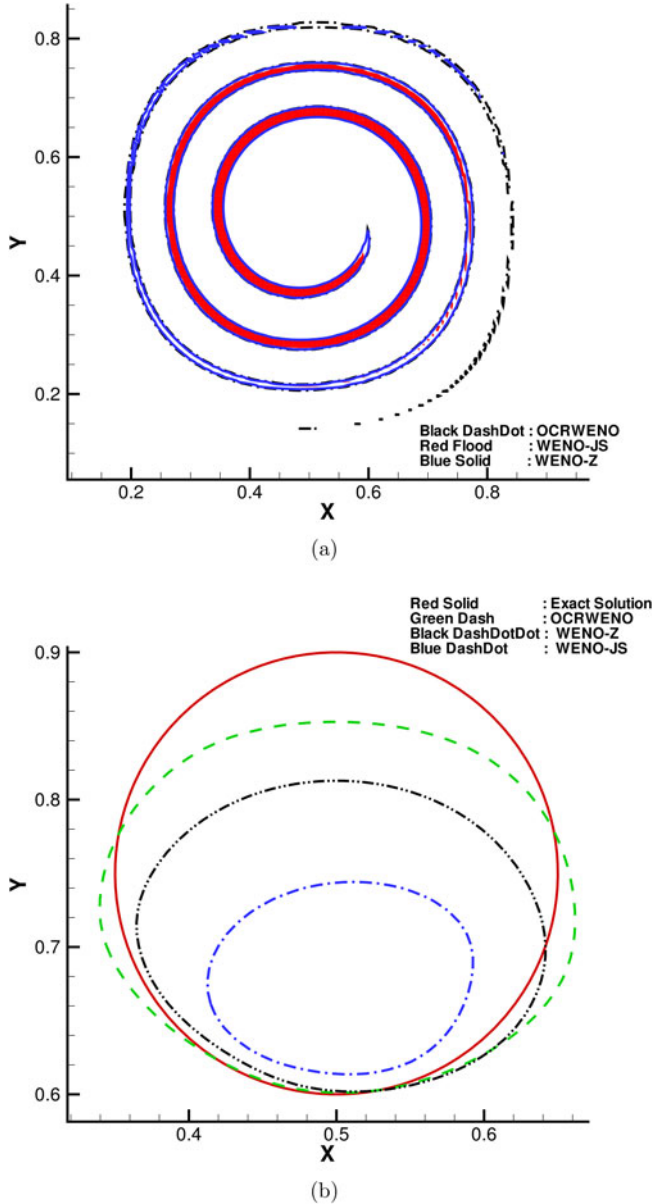
Figure 1. Predicted result of single vortex with $T = 16$. (a) $t = \frac{T}{2} = 8$; (b) $t = T = 16$.

3.2.2. Projection methodology and numerical stability conditions

The projection method described by [60,61] is developed for solving the varying-density incompressible flow along with the incompressibility constraint condition. In this study, approximation of Eq. (10) is based on the projection method. Eq. (10) is rewritten, which uses Adams–Bashforth scheme for time advancement as

$$\frac{\mathbf{u}^{n+1} - \mathbf{u}^n}{\Delta t} + \mathbf{f}^n + \frac{1}{\rho(\phi)} \frac{\delta \mathbf{x}}{\Delta \mathbf{x}} P^{n+\frac{1}{2}} = 0, \tag{60}$$

where $\delta \mathbf{x}$ is the first-order central-difference operator and

$$\mathbf{f}^n = \frac{3}{2} \mathbf{A}^n - \frac{1}{2} \mathbf{A}^{n-1}, \tag{61}$$

with
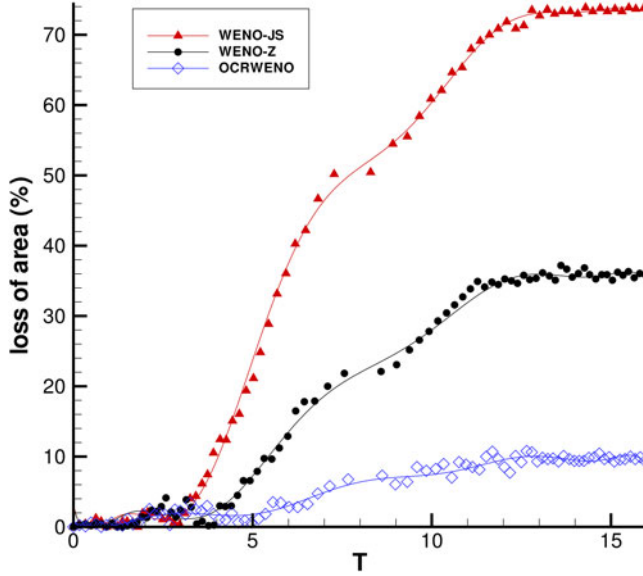
Figure 2. Evolution of area loss of single vortex problem by three distinct schemes.

$$\mathbf{A} = \mathbf{u} \cdot \nabla \mathbf{u} - \frac{1}{\rho(\phi)} \nabla \cdot \left[\mu(\phi) \left(\nabla \mathbf{u} + (\nabla \mathbf{u})^T \right) \right] - \mathbf{g} - \mathbf{f}_{sf}. \tag{62}$$

Taking the divergence operator on both sides of Eq. (60) and using the fact that $\nabla \cdot \mathbf{u}^{n+1} = 0$ derives the Poisson equation

$$\left(\frac{\delta x}{\Delta x} \frac{1}{\rho(\phi)} \frac{\delta x}{\Delta x} + \frac{\delta y}{\Delta y} \frac{1}{\rho(\phi)} \frac{\delta y}{\Delta y} + \frac{\delta z}{\Delta z} \frac{1}{\rho(\phi)} \frac{\delta z}{\Delta z} \right) p^{n+1/2} = \mathbf{RHS}, \tag{63}$$

where $\mathbf{RHS} = \frac{\delta x}{\Delta x} \left(\frac{u^n}{\Delta t} - f^n \right) + \frac{\delta y}{\Delta y} \left(\frac{v^n}{\Delta t} - g^n \right) + \frac{\delta z}{\Delta z} \left(\frac{w^n}{\Delta t} - h^n \right)$. After solving Eq. (60) for p, the updated value $\mathbf{u}^{n+1}$ can be obtained according to Eq. (60).

For the explicit Adams–Bashforth scheme, the time step constraint should be found according to the Courant–Friedrichs–Lewy (CFL) condition. The computational time step Δt at time t^n is limited by the advection, diffusion, gravity and surface tension terms

$$\Delta t^{n+1} \leq \min \left(\Delta t_u, \Delta t_\mu, \Delta t_g, \Delta t_\sigma \right), \tag{64}$$

where $\quad \Delta t_u = \min_\Omega (|\frac{u}{\Delta x}|, |\frac{v}{\Delta y}|, |\frac{w}{\Delta z}|), \quad \Delta t_\mu = \min_{\Omega_\delta} \frac{Re}{2 \left[\frac{1}{\Delta x^2} + \frac{1}{\Delta y^2} + \frac{1}{\Delta z^2} \right]}, \quad \Delta t_g = \min_\Omega \sqrt{\frac{\Delta z}{g}}, \quad$ and

$\Delta t_\sigma = \min_{\Omega_\delta} \sqrt{\frac{(\rho_G + \rho_L) \Delta h^3}{4\pi\sigma}}$, with $\Delta h = \min(\Delta x, \Delta y, \Delta z)$.

3.2.3. Poisson solver

At each interior point (i, j, k), application of a central-difference approximation for the left-hand side of Eq. (63) leads to
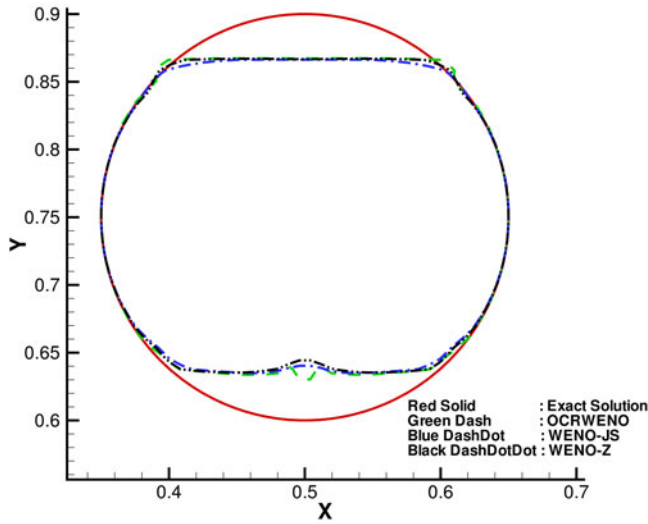
$$aP_{i-1,j,k} + bP_{i+1,j,k} + cP_{i,j,k} + dP_{i,j-1,k} + eP_{i,j+1,k} + fP_{i,j,k-1} + gP_{i,j,k+1} = (\mathbf{RHS})_{i,j,k}, \tag{65}$$

where $\quad a = b = \frac{1}{\rho \Delta x^2}, d = e = \frac{1}{\rho \Delta y^2}, f = g = \frac{1}{\rho \Delta z^2}, \quad$ and $\quad c = -(a + b + d + e + f + g) = -(\frac{1}{\rho \Delta x^2} + \frac{1}{\rho \Delta y^2} + \frac{1}{\rho \Delta z^2})$. The pressure Poisson equation (i.e. Eq. (65)) is solved using the point successive over-relaxation (PSOR) solver

$$P_{i,j,k}^{m+1} = \omega P_{i,j,k}^{m+1} + (1-\omega) P_{i,j,k}^m, \tag{66}$$
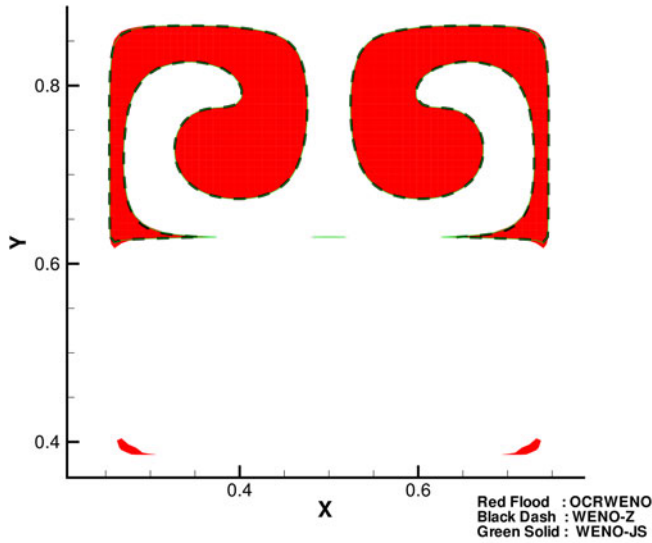
Figure 3. Predicted result of 16 vortices with $T = 2$. (a) $t = \frac{T}{2} = 1$; (b) $t = T = 2$.

where m is the iteration counter, and the coefficient of relaxation ω in this study is chosen to be 1.5. The solver can usually converge to a specified tolerance 10^{-4}

$$|P_{i,j,k}^{m+1} - P_{i,j,k}^m| \leq 10^{-4}. \tag{67}$$

3.3. Summary of the two-phase flow algorithm

We first initialize the level set function by solving Eq. (1). Computational procedures for numerical modeling of two-phase flows for a one-time loop are summarized as follows:

1. Compute the interface curvature $\kappa(\phi)$ in Eq. (12).
2. Calculate the density $\rho(\phi)$ and viscosity $\mu(\phi)$ in Eq. (13).
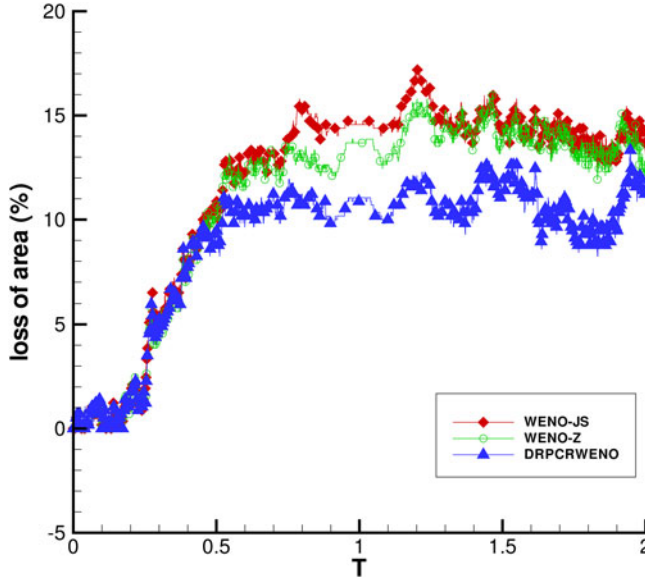
Figure 4. Evolution of area loss of deformation field problem by three distinct schemes.

3. Approximate the convection and diffusion terms in Eq. (10).
4. Solve the pressure Poisson equation (i.e. Eq. (63)) to get pressure solutions.
5. Obtain the new velocity field $\mathbf{u}^{n+1}$ using Eq. (60).
6. Update the level set function using Eq. (14).
7. Re-distance the level set function using Eq. (5).

4. Validation study

To measure the mass conservation property, we define the mass error as

$$\mathbf{M}_{error} = \int_{\Omega} \bar{H}(\phi) \ d\Omega - 1. \tag{68}$$

4.1. Vortex flow

This problem can be used to evaluate the accuracy of the predicted interface advection and deformation. The flow was reversed at $t = \frac{T}{2}$ so that the exact solution obtained at $t = T$ should coincide with its initial solution given by

$$\phi = -\sqrt{(x-0.5)^2 + (y-0.75)^2} + 0.05. \tag{69}$$

The velocity fields are given as

$$u(x, y, t) = \mathbf{sin}^2(\pi x)\mathbf{sin}(2\pi y)\mathbf{cos}(\pi t/T), \tag{70}$$

$$v(x, y, t) = -\mathbf{sin}^2(\pi y)\mathbf{sin}(2\pi x)\mathbf{cos}(\pi t/T). \tag{71}$$

The numerical results obtained using the proposed OCRWENO scheme on a uniform grid of 128×128 are compared with those obtained by WENO-Z [58] and WENO-JS [59] schemes at $T = 16$. In order to demonstrate the advantages of the proposed OCRWENO scheme in preserving the areas of the filaments, the evolution processes of the filaments by using OCRWENO,
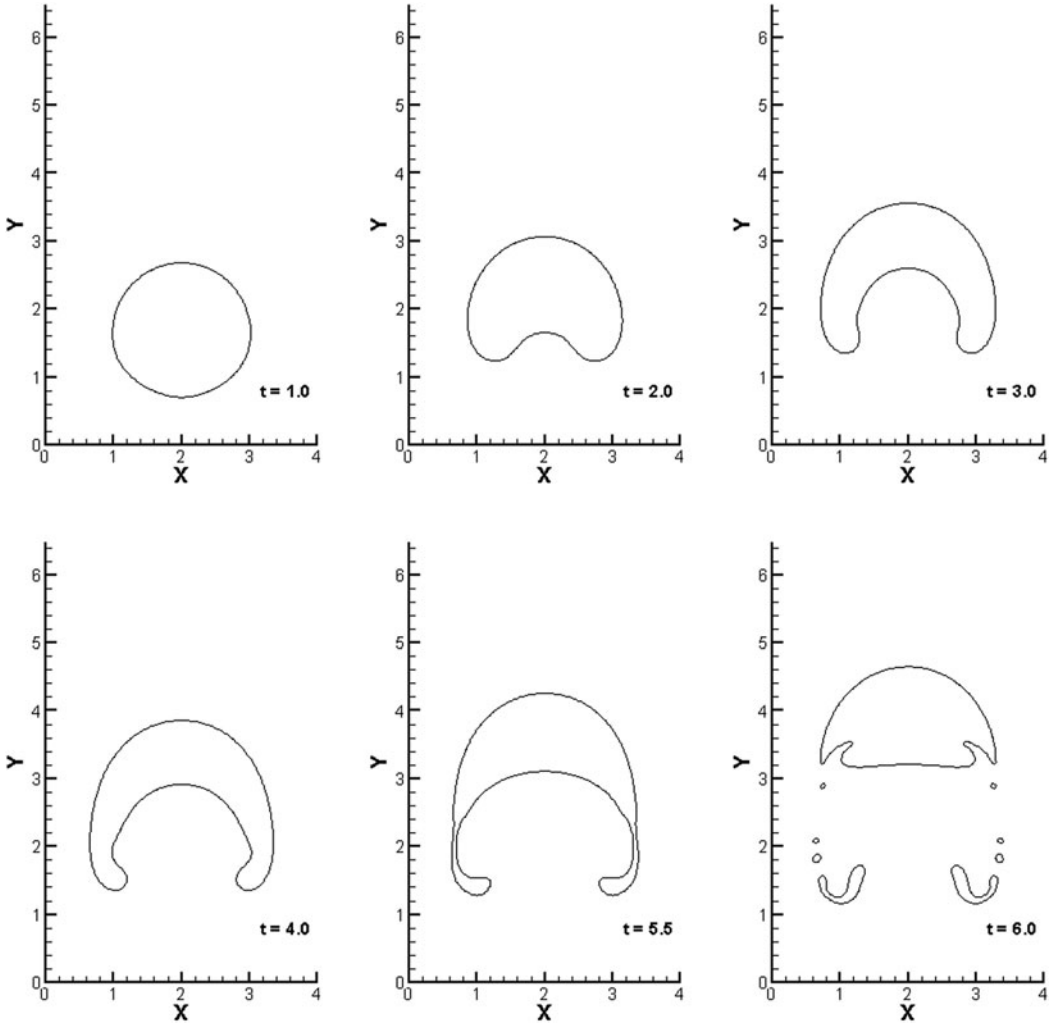
Figure 5. Predicted result of two dimensional single bubble rising problem with $Re = 100$, $We = 200$, $Fr = 1$, $\frac{\mu_g}{\mu_l} = 0.01$ and $\frac{\rho_G}{\rho_L} = 0.2$ in a 4.0×6.48 box with grid 150×243 and time step $\Delta t = 0.01\Delta x$.

WENO-Z and WENO-JS schemes are shown in Figure 1(*a*), from which it can be evidently seen that the proposed OCRWENO can significantly resolve the solution within a thin and elongated filament. Figure 1(*b*) clearly shows that the proposed OCRWENO scheme in this paper can better preserve the areas than the schemes in [58] and [59] do. Mass loss of the vortex flow problem using the different advection schemes on a grid of 128×128 cells is shown in Figure 2.

4.2. Deformation field

An even more sophisticated benchmark test is the one proposed by Smolarkiewicz [36], the entrainment of a circular body in a deformation field determined by 16 vortexes. The periodic velocity field is given by the stream function:

$$\psi = \frac{1}{4\pi} \sin(4\pi(x + 0.5)) \cos(4\pi(y + 0.5)). \tag{72}$$
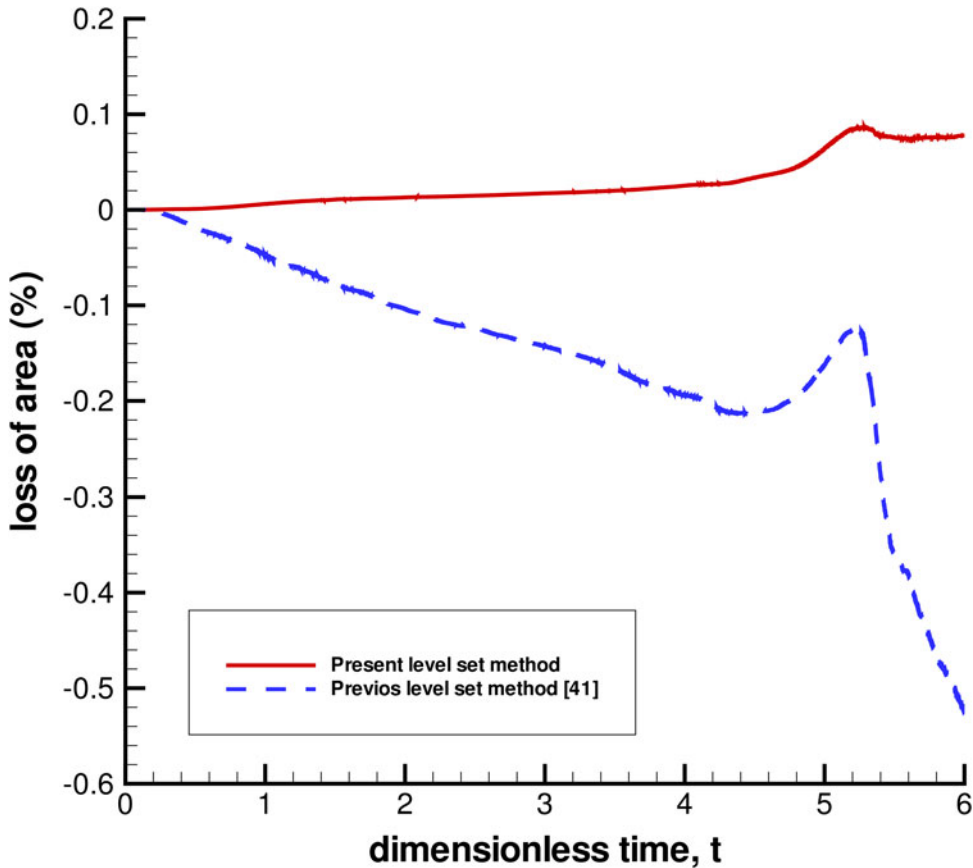
Figure 6. Corresponding area loss of two dimensional single bubble rising problem with $\frac{\rho_G}{\rho_L} = 0.2$.

As suggested in Figure 3, a time-reversed flow field with period $T = 2$ is imposed and the interface crosses the top boundary of the domain to reappear on the bottom at $t = 1$. Figure 3 presents the OCRWENO solutions (in red line), the WENO-Z solutions (in blue line) and the WENO-JS solutions (in green line). As can be seen in Figure 3, the proposed OCRWENO scheme is highly capable in modeling the interface undergoing massive stretching on a grid of 128×128 cells. Figure 4 shows mass loss of the deformation field, in which the fifth-order WENO-Z scheme refers to the one presented in [58] and the fifth-order WENO-JS scheme refers to the one presented in [59]. One can see that the Figure 4 shows better mass property for the proposed OCRWENO scheme.

5. Numerical results of two-phase flow model

5.1. Two dimensional single bubble rising problem

The influence of density on single bubble rising which has been considered by Zhao et al. [62] is also studied in this section. The 4D-in-length and 6.48D-in-height tank is considered here where D is the diameter of the initial bubble. A 1D-in-radius bubble is located 1.48 D above the bottom of the tank. In this study, the Reynolds number (Re), Weber number (We) and density ratio are assumed to be $100, 200, 0.2$ for investigation respectively. The predicted bubble interface in 150×243 grids in shown in Figure 5, which agrees quite well with those by Zhao et al. [62]. In Figure 6, the predicted mass is well conserved using the proposed level set method. Following this, the Reynolds number
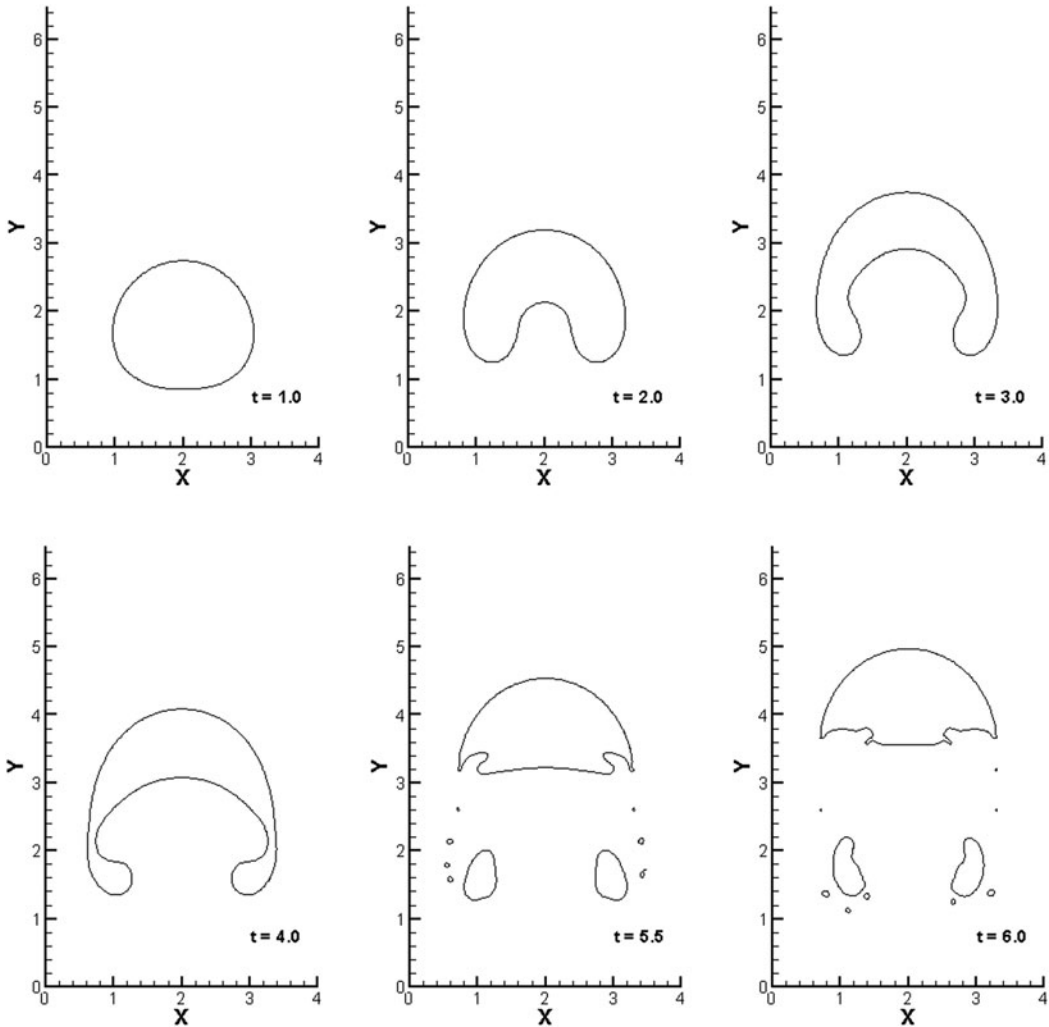
Figure 7. Predicted result of two dimensional single bubble rising problem with $Re = 100$, $We = 200$, $Fr = 1$, $\frac{\mu_G}{\mu_L} = 0.01$ and $\frac{\rho_G}{\rho_L} = 0.01$ in a 4.0×6.48 box with grid 150×243 and time step $\Delta t = 0.01 \Delta x$.

(Re), Weber number (We) and density ratio are assumed to be $100, 200, 0.01$ for next investigation. The predicted bubble interfaces at dimensionless time $t = 1, t = 2, t = 3, t = 4, t = 5.5$ and $t = 6$ also agree well with those in Zhao et al., as is shown in Figure 7 [62]. Comparison between the two investigations in Figures 5 and 7 shows that the decrease in density ratio results in faster rise of the bubble. Figure 8 shows that mass is much better conserved using the proposed level set method compared with that using previous level set method [41].

5.2. Two dimensional bubble bursting at a free surface

Bubble rising in incompressible flows considering buoyancy force has been intensively studied in existing literatures. In this study, a still bubble located at the center of a $3.0D$-wide, $3.5D$-high container is considered where D is the initial diameter of the bubble. The initial water depth in the container is set to $2.5D$. Slip conditions are specified along the horizontal and vertical walls. The density and viscosity ratios of water to air are assumed to be $\frac{\rho_L}{\rho_G} = 0.5$ and $\frac{\mu_L}{\mu_G} = 0.5$. The bubble rising problem is first studied at $Re = \frac{\rho UD}{\nu} = 100$ without considering the buoyancy force,
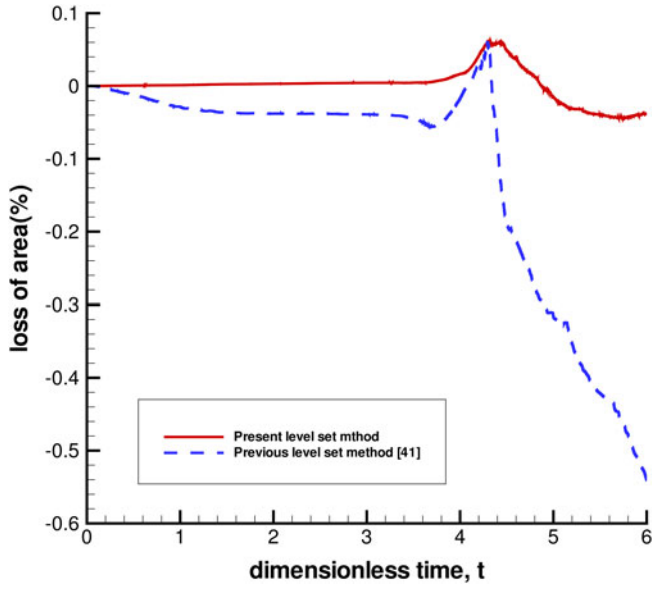
Figure 8. Corresponding area loss of two dimensional single bubble rising problem with $\frac{\rho_G}{\rho_L} = 0.01$.
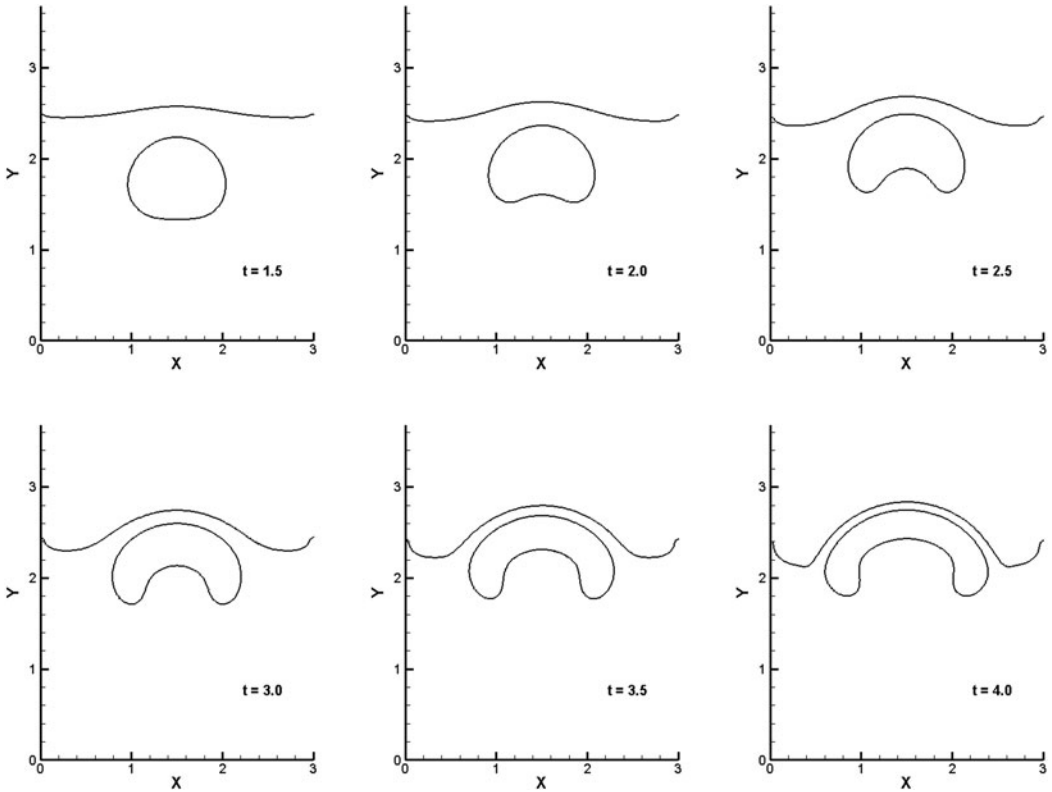

Figure 9. Predicted result of two dimensional single bubble burst at free surface (no surface tension) with $Re = 100$, $Fr = 1$, $\frac{\mu_G}{\mu_L} = 0.5$ and $\frac{\rho_G}{\rho_L} = 0.5$ in a 3×3.5 box with grid 180×210 and time step $\Delta t = 0.01\Delta x$.
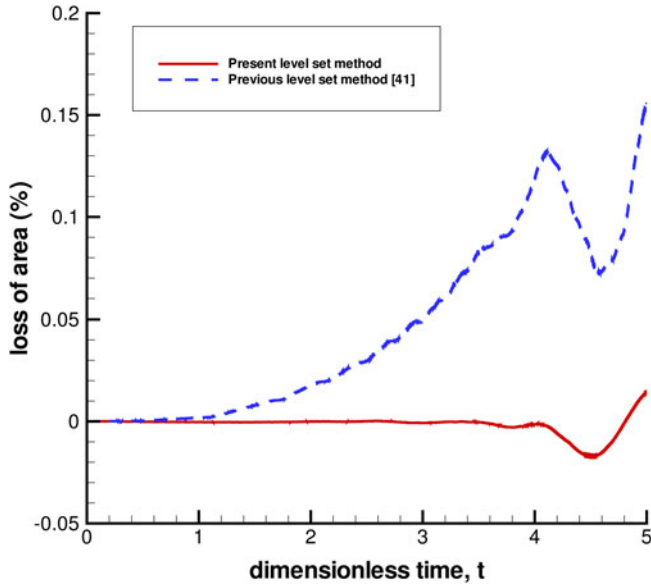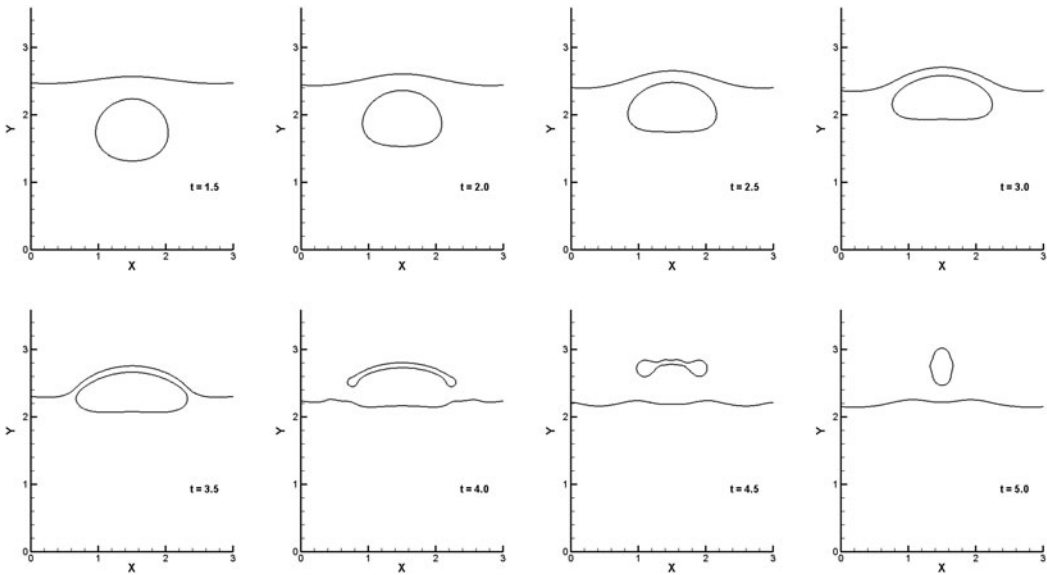
Figure 10. Corresponding area loss of two dimensional bubble burst at free surface (no surface tension).

Figure 11. Predicted result of two dimensional single bubble burst at free surface (with surface tension) with $Re = 100$, $We = 10$, $Fr = 1$, $\frac{\mu_G}{\mu_L} = 0.5$ and $\frac{\rho_G}{\rho_L} = 0.5$ in a 3×3.5 box with grid 180×210 and time step $\Delta t = 0.01 \Delta x$.

where $U = \sqrt{gD}$ is the characteristic velocity. t, x, y are dimensionless variables normalized by U, D, D respectively. Uniform grid sizes of 180×210 and 240×280 are adopted to investigate the effect of grid dependence on the conservative property. The predicted bubble interface and conservative property agree quite well on both the two grids. The simulations, therefore, will only be carried out and shown in 180×210 grids.
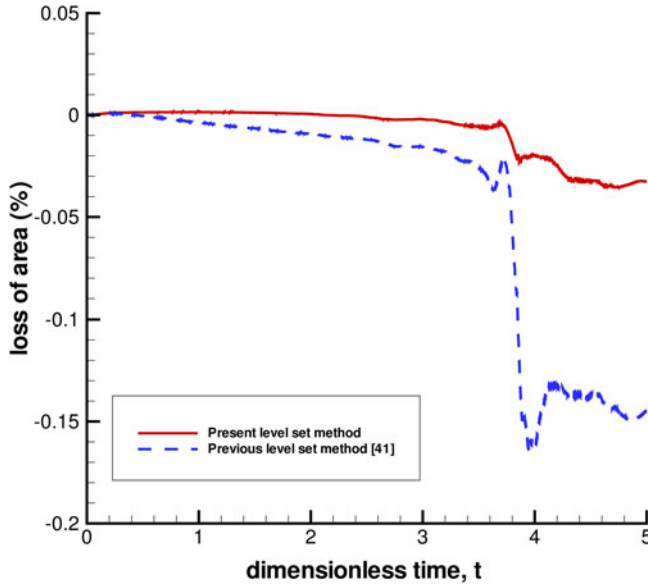
Figure 12. Corresponding area loss of two dimensional bubble burst at free surface (with surface tension).

The predicted bubble interface results are shown in Figure 9. The bubble is deformed to a kidney shape without taking surface tension into account. Figure 10 demonstrates that the mass is conserved quite well using the proposed method. Due to surface tension's ineligible role in bubble rising, this time-evolving bubble problem is simulated by considering the surface tension force in the case of Weber number at $We = \frac{\rho U^2 D}{\sigma} = 10$ and $Re = 100$. The predicted results of bubble rising considering the effect of surface tension force are plotted in Figure 11, which demonstrates good agreement with those of Zhao et al. [62]. It can be seen from Figures 9 and 11 that the effect of surface tension force becomes visual beyond $t = 2.0$. The detailed phenomena of bubble breakup are plotted in Figure 11 in $3.5 \le t \le 4.5$. The conservative property built in the present level set method is still well retained based on the results computed in 180×210 grids in Figure 12.

5.3. Three dimensional single bubble rising problem

The numerical results in [63] of a three-dimensional single bubble rising problem can be used for comparison. In the current calculation, the bubble has a radius $R = 1.0$ and is located in a $6 \times 6 \times 8$ box. $Re = 11.065$, $We = 9.9148$, $Fr = 1$ are assumed in the simulation, with the domain of $90 \times 90 \times 120$ grids. Figure 13 presents the simulation results of the bubble rising problem at dimensionless times $t = 0.8, t = 1.8, t = 2.4$ and $t = 3.6$. In this case, several benchmark parameters including centroid, circularity, and rise velocity are investigated to quantitatively evaluate the capability of the proposed level set method in resolving the rising interface in viscous fluid [64–66]. Translation of the bubble can be measured by the centroid defined as follows:

$$X_c = (x_c, y_c) = \frac{\int_{\Omega_b} \mathbf{x} dx}{\int_{\Omega_b} dx}, \tag{73}$$

where Ω_b refers to the bubble region. It should be noted that x_c is the coordinate of the centroid in x-direction and y_c in y-direction, respectively. Circularity is defined as follows:
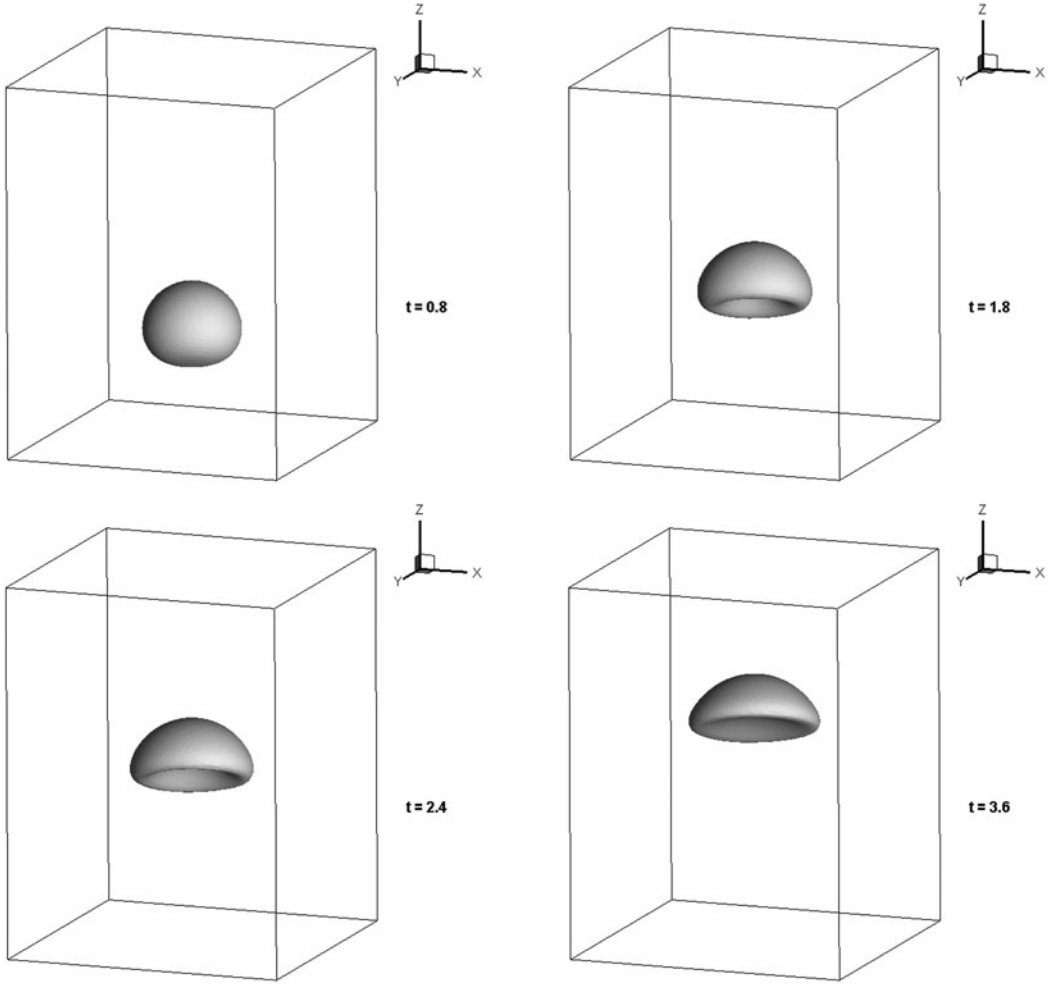
Figure 13. Predicted results of three dimensional single bubble rising benchmark problem. The computation is carried out in a $6 \times 6 \times 8$ cube with grid $90 \times 90 \times 120$, time step $\Delta t = 0.005\Delta x$, $Re = 11.065$, $We = 9.9148$, $Fr = 1$, $\frac{\mu_G}{\mu_L} = \frac{0.01}{1.18}$ and $\frac{\rho_G}{\rho_L} = \frac{0.001}{0.8755}$.

$$C_I = \frac{P_a}{P_b}, \tag{74}$$

where P_a refers to the initial perimeter of the bubble and P_b refers to the perimeter of the bubble at time t. Rise velocity is defined as:

$$V_r = \frac{\int_{\Omega_b} v dy}{\int_{\Omega_b} dy}, \tag{75}$$

where v denotes the velocity magnitude in y-direction. Figure 14 shows benchmark quantities against dimensionless time. Good agreement with the numerical result of rise velocity in Figure 14(a) is clearly demonstrated.

5.4. Three dimensional two-bubble merger problem

The merger of two bubbles both in a coaxial case and an oblique case are simulated in a computational domain of $[0, 4R] \times [0, 4R] \times [0, 8R]$ in this section. The bubble has a radius of $R = 1$, and
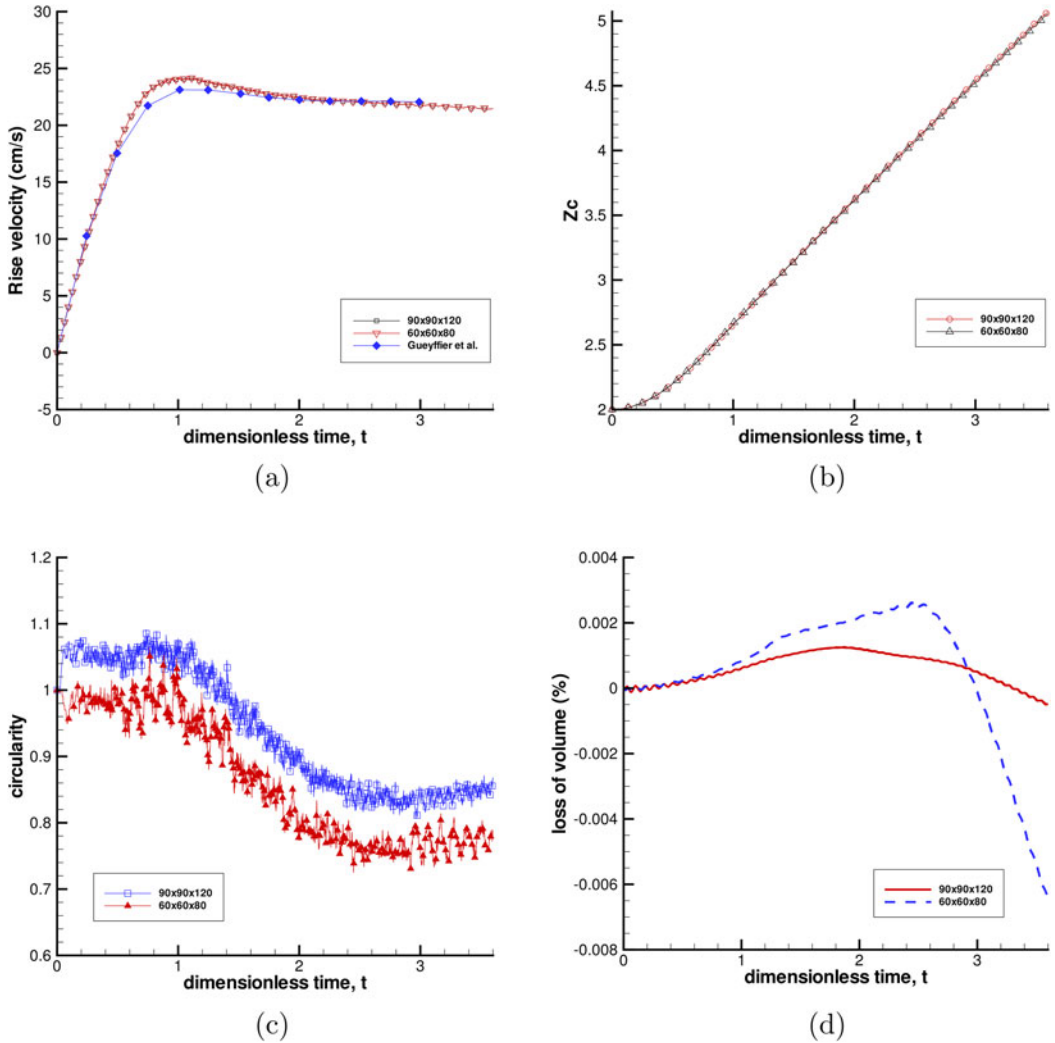
Figure 14. Corresponding benchmark quantities of three dimensional single bubble rising problem. (a) rise velocity, the result is compared with Gueyffier et al. [63]; (b) center of mass; (c) circularity; (d) evolution of volume loss.

$Re = 67.27$, Weber number of $We = 16$, and the Froude number of $Fr = 1$ are assumed [67]. In the coaxial case, center of the upper bubble is located at $(2R, 2R, 2.5R)$ and center of the lower bubble is located at $(2R, 2R, 1R)$ with $80 \times 80 \times 160$ grids. The density and viscosity ratios of water to air are assumed to be $\frac{\rho_L}{\rho_G} = 0.001$ and $\frac{\mu_L}{\mu_G} = 0.01$, respectively. Good agreement can be found in Figures 15 and 16 between this study's simulation results and those of Brereton and Korotney [67], respectively. When the lower bubble enters into the wake region of upper bubble, deformation and acceleration of the lower bubble in z-direction can be seen. In the oblique case, center of the upper bubble is located at $(2R, 2R, 2.5R)$ and center of the lower bubble is located at $(2.85R, 2R, 1R)$. Figures 17 and 18 presents the numerical results in the $80 \times 80 \times 160$ grids, from which solutions obtained from the proposed level set method agree fairly well with those obtained in [67]. In Figure 19, the conservative property built in the present level set method is still well retained for both of the coaxial and oblique bubble rising cases.
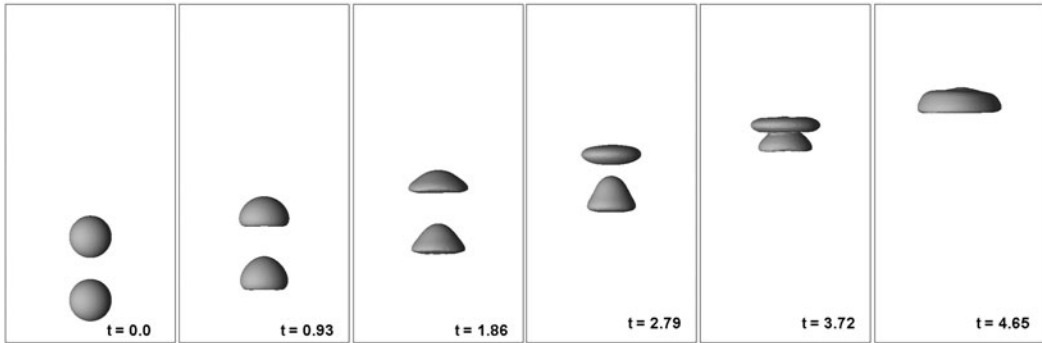
Figure 15. Predicted result of three dimensional two bubble coaxially merger problem. The computation is carried out in a 4 × 4 × 8 cube with grid 80 × 80 × 160, time step $\Delta t = 0.005\Delta x$, $Re = 67.27$, $We = 16$, $Fr = 1$, $\frac{\mu_G}{\mu_L} = 0.01$ and $\frac{\rho_G}{\rho_L} = 0.001$.
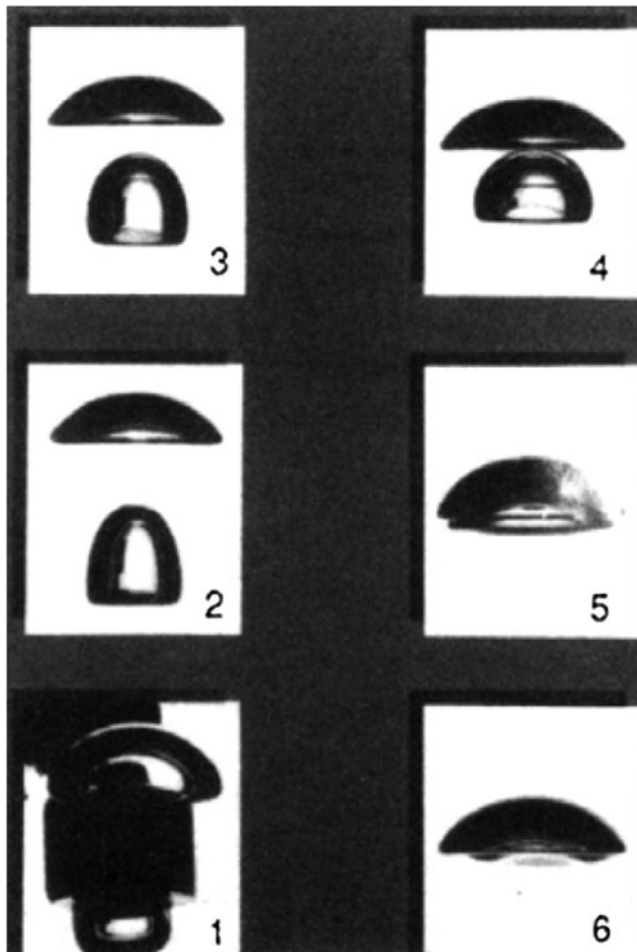

Figure 16. Experiments snapshot [68] of two bubble coaxially merger problem (time difference between the subsequent photographs is 0.03 s).

5.5. Three dimensional bubble bursting at a free surface

Boulton-Stone and Blake [68] has investigated numerical simulation of bubble bursting at a free surface. However, they study concerns only the air bubble bursting phenomena just before the pinch-off liquid jet. In this study, a spherical bubble with unit radius is initially located at
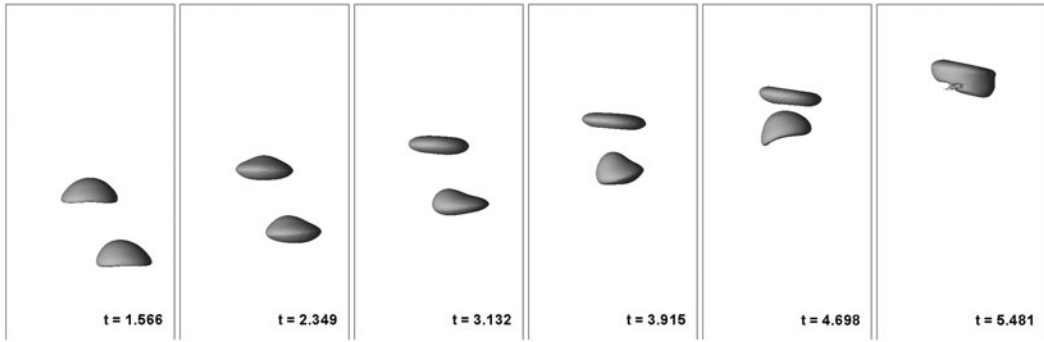
Figure 17. Predicted result of three dimensional two bubble obliquely merger problem. The computation is carried out in a $4 \times 4 \times 8$ cube with grid $80 \times 80 \times 160$, time step $dt = 0.005\Delta x$, $Re = 67.27$, $We = 16$, $Fr = 1$, $\frac{\mu_G}{\mu_L} = 0.01$ and $\frac{\rho_G}{\rho_L} = 0.001$.
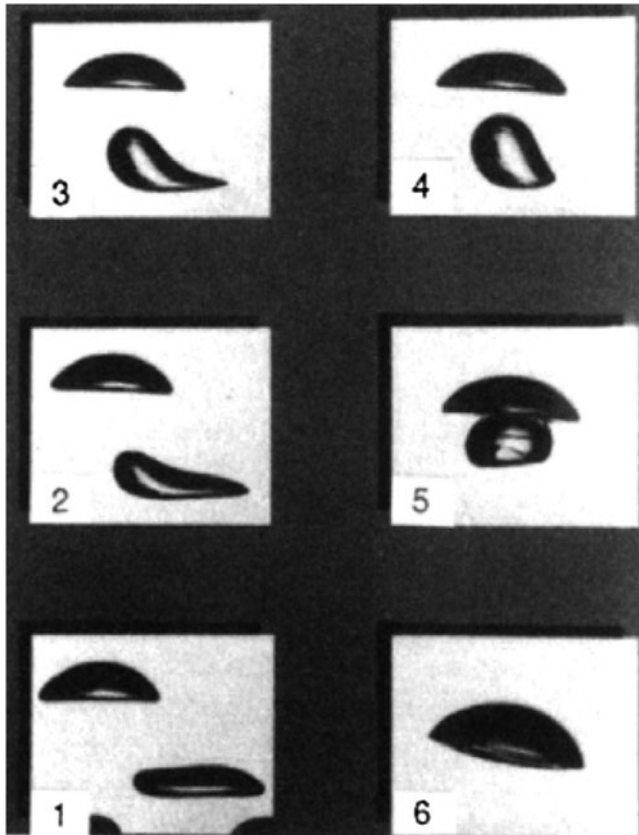

Figure 18. Experiments snapshot [68] of two bubble obliquely merger problem (time difference between the subsequent photographs is 0.03 s).

$(x, y, z) = (0, 0, -3.2)$ in the computational domain of $[-2, 2] \times [-2, 2] \times [-6, 6]$ with $110 \times 110 \times 220$ grids. Non-slip boundary conditions are imposed on the box walls. $Re = 474$, $We = 1$ and $Fr = \frac{U}{\sqrt{gR}} = 0.64$ values are assumed, where R is the characteristic length, radius of spherical bubble. The density and the viscosity ratios of water to air are chosen as 0.001 and 0.01, respectively. Figure 20 presents the numerical solutions obtained at different time. One can see that liquid jet starts breaking up into a droplet at $t = 1.133$ and then the second droplet is formed at $t = 1.8$. As can be evidently seen from the numerical solutions, the pinch-off process of the liquid jet and the generation of liquid droplets after breakup of liquid jet due to capillary instability
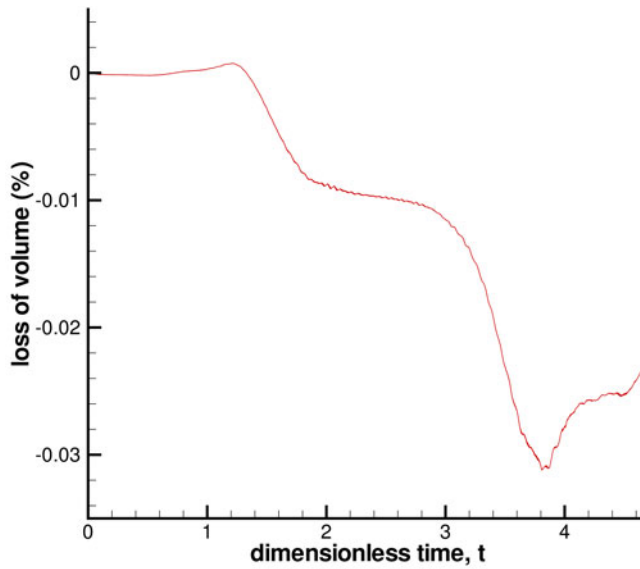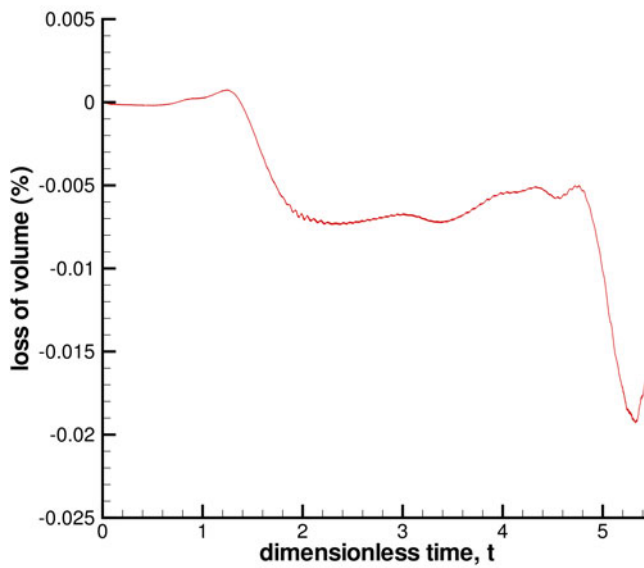
Figure 19. Evolution of volume loss of three dimensional merger problem. (a) coaxially merger; (b) obliquely merger.

have been well captured using the present level set method. We note that the maximum mass error is less than 0.6% of the initial mass.

6. Concluding remarks

We have developed a mass-preserving level set redistancing algorithm to model the incompressible two-phase flow. The level set evolution equation used to advect the evolving interface should preserve its better dispersive property and avoid oscillatory solutions for discontinuities, and the
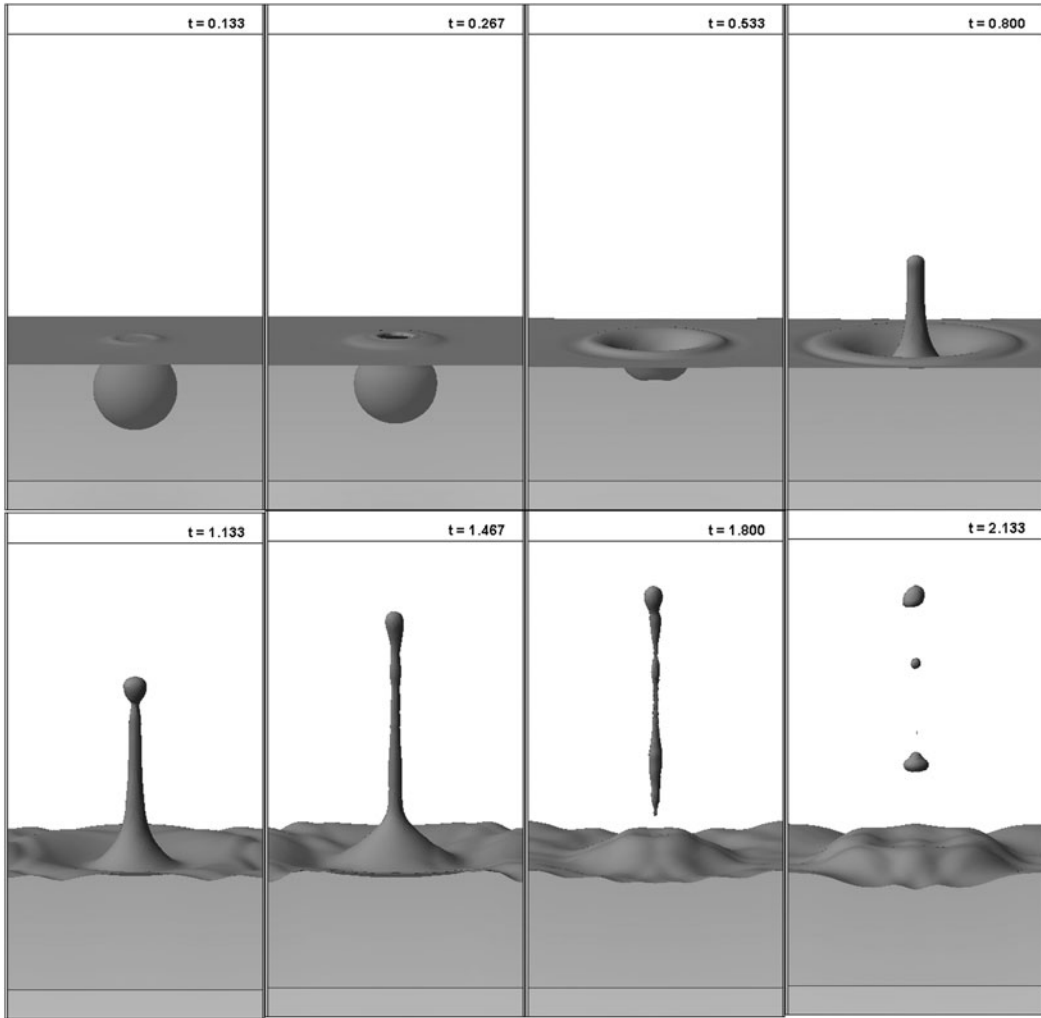
Figure 20. Predicted result of three dimensional bubble burst at the free surface. The computation is carried out in a $6 \times 6 \times 12$ cube with grid $110 \times 110 \times 220$, time step $\Delta t = 0.005\Delta x$, $Re = 474$, $We = 1$, $Fr = 0.64$, $\frac{\mu_G}{\mu_L} = 0.01$ and $\frac{\rho_G}{\rho_L} = 0.001$.

re-initialization equation employed to construct the signed distance function should meanwhile accommodate the conservative interface property. Under these requirements, an optimized compact reconstruction weighted essentially non-oscillatory (OCRWENO) scheme for the computation of level set evolution equation with respect to its accuracy and efficiency in comparison to WENO-JS and WENO-Z schemes is proposed. The reinitialization procedure in the level set method considerably contributes to reducing the mass loss thanks to adding the mass correction term in the simulation. The proposed level set method are tested for simulations of various bubble rising problems with large density differences at different Reynolds and Weber numbers. The predicted results have been shown to agree quite well with experimental results.

Funding

References

[1] Q. L. Ji, X. Z. Zhao, and S. Dong, "Numerical study of violent impact flow using a CIP-Based model," *J. Appl. Math.*, vol. 2013, pp. 1–12, 2013.

[2] I. Chakraborty, G. Biswas, and P. S. Ghoshdastidar, "A coupled level-set and volume-of-fluid method for the buoyant rise of gas bubbles in liquids," *Int. J. Heat Mass Transfer*, vol. 58, no. 1–2, pp. 240–259, 2013.

[3] B. Ningegowda, and B. Premachandran, "A coupled level set and volume of fluid method with multi-directional advection algorithms for two-phase flows with and without phase change," *Int. J. Heat Mass Transfer*, vol. 79, pp. 532–550, 2014.

[4] S. Osher, and R. Fedkiw, *Level Set Methods and Dynamic Implicit Surfaces, Appl. Math. Sci*, vol. 153. New York, NY: Springer-Verlag New York Inc., 2003.

[5] M. Sussman, and E. Fatemi, "An efficient, interface-preserving level set redistancing algorithm and its application to interfacial incompressible fluid flow," *SIAM J. Sci. Comput*, vol. 20, no. 4, pp. 1165–1191, 1999.

[6] A. M. Yang, S. k Chen, L. Yang, and X. Q. Yang, "An upwind finite volume method for incompressible inviscid free surface flows," *Comput. Fluids*, vol. 101, no. 20, pp. 170–182, 2014.

[7] M. Choi, G. Son, and W. Shim, "A level-set method for droplet impact and penetration into a porous medium," *Comput. Fluids*, vol. 145, no. 2, pp. 153–166, 2017.

[8] D. Gaudlitz, and N. A. Adams, "On improving mass-conservation properties of the hybrid particle-level-set method," *Comput. Fluids*, vol. 37, no. 10, pp. 1320–1331, 2008.

[9] G. Son, and V. K. Dhir, "A level set method for analysis of film boiling on an immersed solid surface," *Numer. Heat Transfer B*, vol. 52, no. 2, pp. 153–177, 2007.

[10] H. Hwang, and G. Son, "A level-set method for the direct numerical simulation of particle motion in droplet evaporation," *Numer. Heat Transfer B*, vol. 68, no. 6, pp. 479–494, 2015.

[11] A. Balabel, "Numerical simulation of two-dimensional binary droplets collision outcomes using the level set method," *Int. J. Comput. Fluid D*, vol. 26, no. 1, pp. 1–21, 2012.

[12] M. K. Touré, and A. Soulaïmani, "Stabilized finite element methods for solving the level set equation without reinitialization," *Comput. Math. Appl*, vol. 71, no. 8, pp. 1602–1623, 2016.

[13] Q. Liu, C. K. Chan, and X. L. Cheng, "Simulation of a premixed turbulent flame by a conservative level set method," *Int. J. Comput. Math.*, vol. 88, no. 10, pp. 2154–2166, 2011.

[14] F. Losasso, R. Fedkiw, and S. Osher, "Spatially adaptive techniques for level set methods and incompressible flow," *Comput. Fluids*, vol. 35, no. 10, pp. 995–1010, 2006.

[15] A. Salih, and S. G. Moulic, "A mass conservation scheme for level set method applied to multiphase incompressible flows," *Int. J. Comput. Meth. Eng. Sci. Mech.*, vol. 14, no. 4, pp. 271–289, 2013.

[16] K. Kitamura, and T. Nonomura, "Assessment of WENO-Extended two-fluid modelling in compressible multiphase flows, comput," *Fluids*, vol. 31, no. 3, pp. 188–194, 2017.

[17] S. Kurioka, and D. R. Dowling, "Numerical simulation of free surface flows with the level set method using an extremely high-order accuracy WENO advection scheme," *Int. J. Comput. Fluid D*, vol. 23, no. 3, pp. 233–243, 2009.

[18] M. Oliveira, J. Z. Su, P. Xie, and C. Q. Liu, "Truncation error, dissipation and dispersion terms of fifth order WENO and of WCS for 1D conservation law," *Int. J. Comput. Math*, vol. 87, no. 2, pp. 339–352, 2010.

[19] A. Salih, and S. G. Moulic, "Some numerical studies of interface advection properties of level set method," *Sadhana*, vol. 34, no. 2, pp. 271–298, 2009.

[20] M. P. Martín, E. M. Taylor, M. Wu, and V. G. Weirs, "A bandwidth-optimized WENO scheme for effective direct numerical simulation of compressible turbulence," *J. Comput. Phys*, vol. 220, no. 1, pp. 270–289, 2006.

[21] M. Sussman, and E. G. Puckett, "A coupled level set and volume-of-fluid method for computing 3D and axisymmetric incompressible two-phase flow," *J. Comput. Phys*, vol. 162, no. 2, pp. 301–337, 2000.

[22] K. Yokoi, "A practical numerical framework for free surface flows based on CLSVOF method, multi-moment methods and density-scaled CSF model: Numerical simulations of droplet splashing," *J. Comput. Phys*, vol. 232, no. 1, pp. 252–271, 2013.

[23] G. Son, "Efficient implementation of a coupled level-set and volume-of-fluid method for three dimensional incompressible two-phase flows," *Numer. Heat Transfer B*, vol. 43, no. 6, pp. 549–565, 2003.

[24] W. P. Hong, and Y. B. Wang, "A coupled level set and volume-of-fluid simulation for heat transfer of the double droplet impact on a spherical liquid film," *Numer. Heat Transfer B*, vol. 71, no. 4, pp. 359–371, 2017.

[25] Y. Y. Tsui, C. Y. Liu, and S. W. Lin, "Coupled level-set and volume-of-fluid method for two-phase flow calculations," *Numer. Heat Transfer B*, vol. 71, no. 2, pp. 173–185, 2017.

[26] D. L. Sun, and W. Q. Tao, "A coupled volume-of-fluid and level set (VOSET) method for computing incompressible two-phase flows," *Int. J. Heat Mass Transfer*, vol. 53, no. 4, pp. 645–655, 2010.

[27] T. Wang, H. X. Li, Y. C. Feng, and D. X. Shi, "A coupled volume-of-fluid and level set (VOSET) method on dynamically adaptive quadtree grids," *Int. J. Heat Mass Transfer*, vol. 67, pp. 70–73, 2013.

[28] K. Ling, Z. H. Li, D. L. Sun, Y. L. He, and W. Q. Tao, "A three-dimensional volume of fluid & level set (VOSET) method for incompressible two-phase flow," *Comput. Fluids*, vol. 118, pp. 293–304, 2015.

[29] Z. Z. Cao, D. L. Sun, B. Yu, and J. J. Wei, "A coupled volume-of-fluid and level set (VOSET) method based on remapping algorithm for unstructured triangular grids," *Int. J. Heat Mass Transfer*, vol. 111, pp. 232–245, 2017.

[30] E. Olsson, and G. Kreiss, "A conservative level set method for two phase flow," *J. Comput. Phys.*, vol. 210, no. 1, pp. 225–246, 2005.

[31] C. E. Kees, I. Akkerman, M. W. Farthing, and Y. Bazilevs, "A conservative level set method suitable for variable-order approximations and unstructured meshes," *J. Comput. Phys*, vol. 230, no. 12, pp. 4536–4558, 2011.

[32] L. H. Zhao, J. Mao, X. Bai, X. Q. Liu, T. C. Li, and J. J. R. Williams, "Finite element implementation of an improved conservative level set method for two-phase flow," *Comput. Fluids*, vol. 100, pp. 138–154, 2014.

[33] D. Enright, R. Fedkiw, J. Ferziger, and I. Mitchell, "A hybrid particle level set method for improved interface capturing," *J. Comput. Phys.*, vol. 183, no. 1, pp. 83–116, 2002.

[34] P. J. Archer, and W. Bai, "A new non-overlapping concept to improve the hybrid particle level set method in multi-phase fluid flows," *J. Comput. Phys.*, vol. 282, pp. 317–333, 2015.

[35] Z. Y. Wang, J. M. Yang, and F. Stern, "An improved particle correction procedure for the particle level set method," *J. Comput. Phys.*, vol. 228, no. 16, pp. 5819–5837, 2009.

[36] L. Jiang, F. B. Liu, and D. R. Chen, "A fast particle level set method with optimized particle correction procedure for interface capturing," *J. Comput. Phys.*, vol. 299, pp. 804–819, 2015.

[37] M. Sussman, A. S. Almgren, J. B. Bell, P. Colella, L. H. Howell, and M. L. Welcome, "An adaptive level set approach for incompressible two-phase flows," *J. Comput. Phys.*, vol. 148, no. 1, pp. 81–124, 1999.

[38] R. R. Nourgaliev, S. Wiri, N. T. Dinh, and T. G. Theofanous, "On improving mass conservation of level set by reducing spatial discretization errors," *Int. J. Multiphas. Flow*, vol. 31, no. 12, pp. 1329–1336, 2005.

[39] M. Herrmann, "A balanced force refined level set grid method for two-phase flows on unstructured flow solver grids," *J. Comput. Phys.*, vol. 227, no. 4, pp. 2674–2706, 2008.

[40] R. F. Ausas, E. A. Dari, and G. C. Buscaglia, "A geometric mass-preserving redistancing scheme for the level set function," *Int. J. Numer. Meth. Fluids*, vol. 65, no. 8, pp. 989–1010, 2011.

[41] M. Sussman, P. Smereka, and S. Osher, "A level set approach for computing solutions to incompressible two-phase flow," *J. Comput. Phys.*, vol. 114, no. 1, pp. 146–159, 1994.

[42] J. M. Yang, and F. Stern, "Sharp interface immersed-boundary/level-set method for wave-body interactions," *J. Comput. Phys.*, vol. 228, no. 17, pp. 6590–6616, 2009.

[43] A. Harten, B. Engquist, S. Osher, and S. R. Chakravarthy, "Uniformly high order essentially non-oscillatory schemes III," *J. Comput. Phys.*, vol. 71, no. 2, pp. 231–303, 1987.

[44] G. S. Jiang, and C. W. Shu, "Efficient implementation of weighted ENO schemes," *J. Comput. Phys.*, vol. 126, no. 1, pp. 202–228, 1996.

[45] J. U. Brackbill, D. B. Kothe, and C. Zemach, "A continuum method for modelling surface tension," *J. Comput. Phys*, vol. 100, no. 2, pp. 335–354, 1992.

[46] Y. F. Yap, J. C. Chai, T. N. Wong, K. C. Toh, and H. Y. Zhang, "A global mass correction scheme for the level-set method," *Numer. Heat Transfer B*, vol. 50, no. 5, pp. 455–472, 2006.

[47] S. K. Lele, "Compact finite difference schemes with spectral-Like resolution," *J. Comput. Phys.*, vol. 103, no. 1, pp. 16–42, 1992.

[48] T. K. Sengupta, G. Ganeriwal, and S. De, "Analysis of central and upwind compact schemes," *J. Comput. Phys.*, vol. 192, no. 2, pp. 677–694, 2003.

[49] T. K. Sengupta, S. K. Sircar, and A. Dipankar, "High accuracy schemes for DNS and acoustics," *J. Sci. Comput.*, vol. 26, no. 2, pp. 151–193, 2006.

[50] X. L. Zhong, "High-order finite-difference schemes for numerical simulation of hypersonic boundary-layer transition," *J. Comput. Phys.*, vol. 144, no. 2, pp. 662–709, 1998.

[51] C. K. W. Tam, and J. C. Webb, "Dispersion-relation-preserving finite difference schemes for computational acoustics," *J. Comput. Phys.*, vol. 107, no. 2, pp. 262–281, 1993.

[52] P. H. Chiu, and Y. T. Lin, "A conservative phase field method for solving incompressible two-phase flows," *J. Comput. Phys*, vol. 230, no. 1, pp. 185–204, 2011.

[53] P. H. Chiu, and T. W. H. Sheu, "On the development of a dispersion-relation-preserving dual-compact upwind scheme for convection-diffusion equation," *J. Comput. Phys.*, vol. 228, no. 10, pp. 3640–3655, 2009.

[54] Y. G. Bhumkar, T. W. H. Sheu, and T. K. Sengupta, "A dispersion relation preserving optimized upwind compact difference scheme for high accuracy flow simulations," *J. Comput. Phys*, vol. 278, pp. 378–399, 2014.

[55] C. H. Yu, Y. G. Bhumkar, and T. W. H. Sheu, "Dispersion relation preserving combined compact difference schemes for flow problems," *J. Sci. Comput.*, vol. 62, no. 2, pp. 482–516, 2015.

[56] C. W. Shu, "High order WENO and DG methods for time-dependent convection-dominated PDEs: A brief survey of several recent developments," *J. Comput. Phys*, vol. 316, pp. 598–613, 2016.

[57] D. Ghosh, and J. D. Baeder, "Compact reconstruction schemes with weighted ENO limiting for hyperbolic conservation laws," *SIAM J. Sci. Comput.*, vol. 34, no. 3, pp. A1678–A1706, 2012.

[58] R. Borges, M. Carmona, B. Costa, and W. S. Don, "An improved weighted essentially non-oscillatory scheme for hyperbolic conservation laws," *J. Comput. Phys.*, vol. 227, no. 6, pp. 3191–3211, 2008.

[59] G. S. Jiang, and D. P. Peng, "Weighted ENO schemes for Hamilton-Jacobi equations," *SIAM J. Sci. Comput.*, vol. 21, no. 6, pp. 2126–2143, 2000.

[60] A. S. Almgren, J. B. Bell, and W. G. Szymczak, "A numerical method for the incompressible Navier-Stokes equations based on an approximate projection," *SIAM J. Sci. Comput*, vol. 17, no. 2, pp. 358–369, 1996.

[61] E. G. Puckett, A. S. Almgren, J. B. Bell, D. L. Marcus, and W. J. Rider, "A high-order projection method for tracking fluid interfaces in variable density incompressible flows," *J. Comput. Phys.*, vol. 130, no. 2, pp. 269–282, 1997.

[62] Y. Zhao, H. H. Tan, and B. L. Zhang, "A high-resolution characteristics-based implicit dual time-stepping VOF method for free surface flow simulation on unstructured grids," *J. Comput. Phys.*, vol. 183, no. 1, pp. 233–273, 2002.

[63] D. Gueyffier, J. Li, A. Nadim, R. Scardovelli, and S. Zaleski, "Volume-of-fluid interface tracking with smoothed surface stress methods for three-dimensional flows," *J. Comput. Phys*, vol. 152, no. 2, pp. 423–456, 1999.

[64] J. Klostermann, K. Schaake, and R. Schwarze, "Numerical simulation of a single rising bubble by VOF with surface compression," *Int. J. Numer. Meth. Fluids*, vol. 71, no. 8, pp. 960–982, 2013.

[65] S. Hysing *et al.*, "Quantitative benchmark computations of two-dimensional bubble dynamics," *Int. J. Numer. Meth. Fluids*, vol. 60, no. 11, pp. 1259–1288, 2009.

[66] J. S. Hua, and J. Lou, "Numerical simulation of bubble rising in viscous liquid," *J. Comput. Phys.*, vol. 222, no. 2, pp. 769–795, 2007.

[67] G. Brereton, and D. Korotney, "Coaxial and oblique coalescence of two rising bubbles," in *Dynamics of Bubbles and Vortices near a Free Surface*, I. Sahin and G. Tryggvason, Eds. New York, NY: ASME, 1991.

[68] J. M. Boulton-Stone, and J. R. Blake, "Gas bubbles bursting at a free surface," *J. Fluid Mech.*, vol. 254, no. 1, pp. 437–466, 1993.